Available online at www.sciencedirect.com

ScienceDirect

Geochimica et Cosmochimica Acta 304 (2021) 234–257

Geochimica et Cosmochimica Acta

www.elsevier.com/locate/gca

In situ Si isotope and chemical constraints on formation and processing of chondrules in the Allende meteorite

Yogita Kadlag [a,b,*], Michael Tatzel [a,c,d], Daniel A. Frick [c], Harry Becker [a], Philipp Kühne [a]

[a] *Freie Universität Berlin, Institut für Geologische Wissenschaften, Malteserstr. 74-100, 12249 Berlin, Germany*
[b] *Universität Bern, Physikalisches Institut, Sidlerstrasse 5, 3012 Bern, Switzerland*
[c] *GFZ German Research Centre for Geosciences, Telegrafenberg, 14473 Potsdam, Germany*
[d] *Universität Göttingen, Geowissenschaftliches Zentrum, Goldschmidtstr. 1, 37077 Göttingen, Germany*

Received 29 May 2020; accepted in revised form 13 April 2021; Available online 23 April 2021

Abstract

Chondrules in undifferentiated meteorites are former silicate melt droplets of variable texture and composition. Although widely studied, the chondrule formation mechanisms and conditions that explain all properties of chondrules are yet to be identified. To further constrain the processes that affected chondrules in the solar nebula and on the meteorite parent body, we determined *in situ* Si isotope ratios and major and trace element compositions of minerals in chondrules of variable types and sizes from the Allende CV3 chondrite.

The δ^{30}Si in chondrule minerals ranges from -1.28 ± 0.19 to 0.55 ± 0.20‰ (2SE). The δ^{30}Si in chondrules shows no direct relationship with chondrule sizes or with distance between core and rim. Barred olivine-rich chondrules record the highest δ^{30}Si, likely because of faster cooling and less interaction with isotopically light nebular gas. Type I non-porphyritic and some porphyritic chondrules show overall higher δ^{30}Si compared to type II porphyritic chondrules. Furthermore, Mg-rich olivine and Mg-rich pyroxene have systematically higher δ^{30}Si compared to Fe-rich olivine and Fe-rich pyroxene.

The variable δ^{30}Si of type I chondrule silicates (Mg-rich) compared to type II chondrule silicates (Fe-rich) may be explained by variable interaction of chondrule silicates with the nebular gas in the solar nebula. We envision a combination of equilibrium and kinetic isotope fractionation of Si between nebular gas and Fe-poor silicates (such as forsterite, anorthite, enstatite and mesostasis) and Fe-rich olivine and orthopyroxene. Petrographic evidence suggests that the enrichment of Fe in some highly altered porphyritic chondrules and at chondrule rims was likely caused by hydrothermal alteration on the parent body. Therefore, the correlation of Fe and δ^{30}Si of the chondrule minerals might serve as an indicator for the extent of further secondary processing of some chondrule minerals. The sum of these observations suggests that the formation and alteration of type II chondrules occurred by oxidation of originally reduced, metal-rich type I chondrules, both in the solar nebula and later on the meteorite parent body. Remaining ^{30}Si depleted gas contributed to the isotopic composition of matrix silicates. The evidence favours the formation of chondrules and matrix of the Allende meteorite in nebular settings rather than by asteroid impacts.

Keywords: Chondrules; Si isotopes; MC-ICP-MS

* Corresponding author at: Universität Bern, Physikalisches Institut, Sidlerstrasse 5, 3012 Bern, Switzerland
E-mail address: yogita.kadlag@space.unibe.ch (Y. Kadlag).

https://doi.org/10.1016/j.gca.2021.04.022
0016-7037/

1. INTRODUCTION

Chondrules, few hundred microns to mm- sized silicate spheres, are one of the major constituents of undifferentiated meteorites, contributing 15–70 vol% to all but CI carbonaceous chondrites (Scott and Krot, 2003). Various models of chondrule formation were proposed such as the X-wind model, gravitational instability driven by shocks, bow shocks from planetesimals or lightning in the solar nebula, and hypervelocity impact (Shu et al., 1997; Iida et al., 2001; Ciesla and Hood, 2002; Desch and Connolly, 2002; Morris and Desch, 2010; Johnson et al., 2015). However, no single model explains all experimental and observational data on textures, chemical compositions, and isotope records of chondrules (Desch et al., 2012). Thus, conditions and mechanisms of chondrule formation are highly debated since decades (Boss, 1996 and references therein). Element ratios (Mg/Si, Fe/Mg) and isotope ratios of various elements (W, Cr, Mg, Fe, Si, O) in chondrules appear to support the chondrule formation from variably processed dust in the solar nebula (Cohen et al., 2004; Chaussidon et al., 2008; Hezel and Palme, 2010; Hezel et al., 2010; Budde et al., 2016; Friend et al., 2016; Olsen et al., 2016).

Chondrules are mainly composed of olivine and pyroxene, and thus abundances and isotope compositions of their major elements Si, O, Mg and Fe potentially contain important information on nebular and parent body processing of chondrules. Previous studies suggest that the stable isotope variations of Si, O, Mg and Fe in chondrule minerals arise from high temperature processing of chondrule minerals, gas-melt interaction in the solar nebula, and during parent body alteration processes (Young et al., 2002; Chaussidon et al., 2008; Hezel et al., 2010; Kereszturi et al., 2014; Harju et al., 2015; Friend et al., 2016; Villeneuve et al., 2020).

Previous Si isotope data from individual chondrules of carbonaceous chondrites show large variations in δ^{30}Si from −1.14‰ to 1.19‰ (Molini-Velsko et al., 1983; Hezel et al., 2010; Armytage, 2011). While the large uncertainties (±0.4‰) associated with some of the early data limits the interpretation of the apparently large δ^{30}Si range, the favored explanation is evaporation and re-condensation processes and open-system isotope exchange during chondrule formation. During the latter processes, pyroxenes likely formed by reaction of olivine with nebular gas (Krot et al., 2004b; Libourel et al., 2006; Chaussidon et al., 2008; Hezel and Palme, 2010; Friend et al., 2016), and this may have further modified δ^{30}Si values of pyroxenes during cooling (Harju et al., 2015), similarly as for O isotopes (Chaussidon et al., 2008; Tissandier et al., 2002). Lower δ^{30}Si of pyroxenes compared to olivines in type 1AB chondrules (type 1 chondrules contain mainly Mg-rich olivine (A) and Mg-rich pyroxene (B)) from Allende (CV3) and EET 87747 (CR2) were interpreted to reflect preferential incorporation of isotopically light Si from gas into pyroxenes (Harju et al., 2015). However, not all type 1A chondrules (containing primarily Mg-rich olivine) are isotopically heavier than type 1AB chondrules (Armytage et al., 2011), which might indicate isotopic heterogeneity of the chondrule precursors. On the other hand, initial heterogeneity of Si isotopes in chondrule precursors was ruled out in previous studies due to limited Si isotopic variations compared to CAIs (Molini-Velsko et al., 1983; Hezel et al., 2010; Armytage et al., 2011).

Previous experimental studies suggested that different chondrule textures (such as porphyritic, barred and radial textures) can be a consequence of variable cooling rates. The order of cooling rates in chondrules of different textures is, porphyritic < barred < radial (Hewins et al., 1981; Lofgren and Russell, 1986). The impact of the differences in the cooling rates on the stable isotope fractionation in chondrule minerals was not studied in detail yet.

A systematic inverse relationship between δ^{30}Si and chondrule size in Dhajala (H 3.8) observed by Clayton et al. (1983) suggests a role of partial evaporation of Si from chondrules or compositional variations in precursor material. Thus, different formation settings, physical and chemical processes during the formation and cooling of chondrules, as well as alteration on the meteorite parent bodies may be reflected in the stable isotope ratios and abundances of major and trace elements in chondrules (Misawa and Nakamura, 1988; Hezel and Palme, 2008, 2010; Hezel et al., 2010; Armytage et al., 2014; Harju, 2015; Pringle et al., 2017). Understanding the role of isotopic heterogeneity in the precursor material, kinetic or equilibrium fractionation during evaporation and re-condensation processes, isotope-exchange during gas-melt interaction in the solar nebula and during parent body alteration processes for δ^{30}Si in chondrules and their minerals would benefit from data obtained on chondrule phases at high spatial resolution. Here, we present *in situ* silicon isotope ratios and corresponding major, minor and trace element abundances of chondrule silicates from 21 chondrules of different types and sizes from the carbonaceous chondrite Allende (CV3). The data yield new constraints on relationships between chondrule type, origin of isotopic and chemical variations and heterogeneity of precursor materials.

2. SAMPLES, DESCRIPTION OF CHONDRULES AND METHODS

2.1. Samples

All chondrules analyzed in this study are from a thin section (area ~ 4.9 cm^2) of the mildly shocked (S1) Allende meteorite, a member of the oxidized CV subgroup (McSween, 1977) and petrologic type 3.2 (Guimon et al., 1995) or 3.6 (Huss and Lewis, 1994) or > 3.6 (Bonal et al., 2006), corresponding to metamorphic temperatures of ≥ 873 K. Twenty-one chondrules of different textures and types were selected following the classification from Gooding and Keil (1981). Chemical compositions, mineralogy, and a brief description of the chondrules are given in the following sections and are summarized in Tables 1 and 2.

2.2. Description of chondrules

2.2.1. Non-porphyritic chondrules

Three barred olivine chondrules (BOC), a chondrule with composite textures (CTC) and a radial pyroxene chondrule (RPC) were selected for Si isotope analysis (Fig. 1).

Table 1
Major and minor element concentrations and $\delta^{30}Si$ values of non-porphyritic chondrules in the Allende CV3 chondrite analysed by fs-LA-ICP-MS. Chondrule texutre/type, size and location of analysed spots in the chondrule is given (also shown in the supplementary Figs. 1–3).

Analysis ID	Type / Texture	Chondrule size	Analysed phase	Distance from rim (mm)	K (μg/g)	Co (μg/g)	Mg (wt.%)	Ca (wt.%)	Mn (wt.%)	Al (wt.%)	Si (wt.%)	Fe (wt.%)	Ni (wt.%)	Na (wt.%)	$\delta^{29}Si$ (‰)	2 SE	$\delta^{30}Si$ (‰)	2 SE
	BOC																	
CH2-1	**type I/BO**	**1 mm**	Mes	0.35	1027	49	13.1	7.4	0.05	9.2	21.2	1.8	0.12	1.08	−0.05	0.12	−0.23	0.16
CH2-3			Fo	0.08	802	62	29.0	0.9	0.03	1.6	20.4	1.7	0.17	0.56	0.25	0.18	0.55	0.20
CH2-4			Fo + Mes	0.25	665	108	23.1	3.6	0.05	5.5	18.8	2.7	0.31	0.88	0.18	0.20	0.46	0.19
CH8-2	**type I/BO**	**1.1 mm**	Ol + Fo + Mes	0.18	1393	233	18.8	3.8	0.06	5.8	20.4	3.9	0.62	1.79	0.09	0.17	0.12	0.10
CH8-3			Fo + Mes	0.42	2646	215	18.5	6.4	0.04	6.9	20.4	1.3	0.25	0.52	0.10	0.18	0.27	0.13
CH8-4			Ol + Fo + Mes	0.16	1176	95	17.0	5.9	0.03	6.4	20.8	2.6	0.22	1.74	0.14	0.16	0.21	0.11
CH8-5			Ol + Fo	0.05	188	119	26.2	0.9	0.07	0.8	19.8	7.9	0.31	0.11	0.05	0.12	0.08	0.12
CH8-6			Ol + Fo + Mes	0.37	992	49	18.3	6.0	0.04	6.2	21.0	2.0	0.08	0.72	0.25	0.15	0.42	0.12
CH8-7			Fo + Mes	0.11	635	61	19.9	5.9	0.03	5.6	20.6	1.8	0.13	0.51	0.19	0.15	0.19	0.13
CH11-1	**type I/BO**	**1.4 mm**	Ol + Mes +Fo	0.15	1094	91	14.3	6.6	0.04	7.6	21.1	3.7	0.20	1.07	0.04	0.13	0.24	0.16
CH11-3			Ol	0.39	563	177	17.8	1.8	0.10	2.6	18.2	17.2	0.32	0.30	−0.18	0.16	−0.38	0.18
CH11-4			Mes	0.11	489	28	5.6	12.3	0.04	12.7	21.3	0.9	0.12	0.99	0.03	0.14	0.23	0.18
CH13-1	**type II/BO**	**1.3 mm**	Ol	0.02	42	154	20.1	0.4	0.10	1.0	16.4	21.5	0.11	0.03	−0.07	0.10	−0.29	0.12
CH13-2			Ol + Mes	0.43	172	216	18.5	3.7	0.04	4.8	17.1	12.7	0.34	0.15	−0.19	0.16	−0.13	0.15
CH13-3			Ol + Mes +Fo	0.18	52	157	17.1	2.6	0.07	1.8	16.8	21.3	0.17	0.03	−0.16	0.10	−0.27	0.12
CH13-5			Ol + Mes +Fo	0.2	30	64	24.0	1.5	0.04	1.4	17.1	13.8	0.06	0.06	0.00	0.14	0.02	0.14
CH13-6			Ol + Mes +Fo	0.63		21	25.0	2.0	0.03	2.3	19.3	7.3	0.02	0.09	−0.25	0.13	−0.39	0.17
CH16-1	**type II/BO**	**1 mm**	Fo + Px	0.12	1086	129	22.5	2.2	0.07	3.5	20.5	5.1	0.49	0.86	0.14	0.15	0.24	0.13
CH16-2			Fo + Px	0.37	1721	304	22.5	2.4	0.08	4.4	19.7	4.0	0.78	1.23	0.07	0.12	0.02	0.12
CH16-3			Ol	0.05	102	165	23.0	0.4	0.10	0.5	17.1	17.3	0.29	0.09	−0.18	0.11	−0.12	0.14
CH3-2	**RPC**	**0.9 mm**	Px	0.06	866	335	19.2	3.4	0.07	3.8	20.0	8.7	0.54	0.36	0.07	0.19	0.13	0.16
CH3-3			Px	0.27	669	68	19.0	5.1	0.04	4.6	22.7	1.8	0.19	0.27	−0.08	0.21	−0.13	0.15
CH3-4			Px	0.02	550	236	19.1	4.8	0.06	4.0	20.5	5.8	0.88	0.23	−0.12	0.21	−0.35	0.16
CH3-6			Px	0.09	802	66	19.0	4.4	0.05	4.5	22.8	2.5	0.22	0.34	0.01	0.19	0.03	0.15
CH3-7			Px	0.16	832	134	19.9	4.9	0.05	4.0	22.3	2.4	0.34	0.25	0.01	0.17	−0.13	0.15

Precisions of element mass fractions are better than 10% (1 SE).
The long-term external reproducibility $\delta^{30}Si$ values is <0.23‰, 2 SE). bdl = below detection limit.
Ol = olivine (Mg, Fe)$_2SiO_4$, Fo = forsterite (Mg_2SiO_4), Mes = mesostasis (variable mixture of pyroxene, feldspar and glass), Px = pyroxene, alt = alteration veins.

Table 2
Major and minor element concentrations and $\delta^{30}Si$ values of porphyritic chondrules in the Allende CV3 chondrite analysed by fs-LA-ICP-MS. The analytical precision of element concentrations is less than 10% (1 SE). The long-term external reproducibility of $\delta^{30}Si$ values is < 0.23‰, (2SE).

Analysis ID	Type / Texture	Chondrule size	Analysed phase	Distance from rim (mm)	K (μg/g)	Co (μg/g)	Mg (wt.%)	Ca (wt.%)	Mn (wt.%)	Al (wt.%)	Si (wt.%)	Fe (wt.%)	Ni (wt.%)	Na (wt.%)	$\delta^{29}Si$ (‰)	2 SE	$\delta^{30}Si$ (‰)	2 SE
CH4-1	**Type I/POP**	**1 mm**	Fo +Mes +Ol	0.12	614	200	24.2	2.03	0.05	2.37	19.0	7.6	0.32	0.79	−0.09	0.20	−0.16	0.17
CH4-2			Fo + Mes	0.44	352	38	24.3	3.49	0.02	3.69	20.9	1.5	0.05	0.31	0.29	0.13	0.32	0.19
CH4-3			Mes	0.28	545	28	11.0	10.17	0.04	10.39	19.9	1.8	0.04	1.05	−0.23	0.15	−0.68	0.20
CH4-4			Fo + Mes +Ol	0.05	1646	48	23.2	1.83	0.05	2.74	20.4	5.9	0.07	1.17	0.01	0.12	−0.11	0.13
CH4-6			Fo + Mes +Ol	0.09	853	70	20.0	3.56	0.04	4.45	19.9	5.7	0.13	1.88	−0.18	0.13	−0.43	0.14
CH4-7			Fo +Mes	0.38	58	23	25.1	4.13	0.02	4.31	19.5	1.4	0.02	0.16	0.09	0.13	0.05	0.16
CH4-8			Ol + Mes	0.14	1807	845	12.2	3.93	0.07	5.61	16.5	17.2	2.01	1.42	−0.14	0.21	−0.32	0.17
CH5-2	**Type I/POP**	**1.1 mm**	Mes	0.13	729	377	14.2	2.59	0.15	6.24	19.8	11.4	1.43	0.40	−0.43	0.17	−0.83	0.11
CH5-3			Fo	0.37	238	27	29.5	0.69	0.08	0.72	20.2	3.6	0.06	0.19	0.13	0.19	0.13	0.17
CH5-4			Mes +Ol	0.05	255	322	16.0	1.71	0.12	4.42	21.4	10.2	1.05	0.74	−0.32	0.17	−0.62	0.13
CH5-5			Fo + Mes +Ol	0.16	335	86	26.7	1.20	0.09	1.30	20.1	5.5	0.28	0.25	0.10	0.16	0.04	0.13
CH5-6			Ol	0.03	410	402	14.2	1.53	0.13	2.61	16.7	23.1	1.17	0.16	−0.29	0.14	−0.76	0.12
CH10-2	**Type I/PP**	**1.3 mm**	Fo	0.12	171	48	24.7	0.70	0.14	0.72	23.4	4.4	0.13	0.04	−0.22	0.15	−0.57	0.14
CH10-3			Mes +Ol	0.43	619	128	13.1	5.46	0.13	6.16	23.2	3.1	0.44	2.80	−0.15	0.14	−0.45	0.13
CH10-4			Mes +Ol	0.38	522	121	16.7	3.38	0.12	4.48	23.9	3.6	0.56	1.18	−0.17	0.15	−0.37	0.16
CH10-5			Ol	0.05	149	78	20.6	0.86	0.16	1.11	24.2	7.5	0.17	0.05	−0.32	0.13	−0.37	0.12
CH10-6			Px	0.23	220	32	25.0	0.72	0.13	0.89	23.6	3.5	0.07	0.09	−0.08	0.16	−0.16	0.15
CH10-7			Ol	0.05	100	59	21.8	0.64	0.16	0.80	23.7	7.6	0.08	0.03	−0.26	0.12	−0.59	0.13
CH7-1	**Type I/PO**	**0.96 mm**	Fo	0.07	bdl	44	30.7	0.41	0.03	0.22	20.1	3.6	0.05	0.01	0.16	0.16	0.07	0.13
CH7-2			Mes	0.31	214	255	19.8	2.30	0.07	1.41	17.9	16.9	0.45	0.05	−0.24	0.17	−0.53	0.16
CH7-3			Fo	0.1	35	45	29.9	0.49	0.04	0.40	20.6	3.4	0.09	0.02	0.05	0.15	0.00	0.14
CH7-5			Ol	0.17	bdl	41	29.7	0.39	0.06	0.29	19.6	5.6	0.04	0.02	0.13	0.13	0.09	0.12
CH15-2	**Type I/PO**	**1.4 mm**	Ol	0.17	83	75	28.9	0.43	0.07	0.61	19.1	6.8	0.12	0.03	−0.15	0.14	−0.35	0.17
CH15-3			Mes	0.38	456	24	17.8	6.61	0.02	6.84	20.8	1.6	0.05	0.56	0.00	0.15	0.11	0.16
CH15-4			Ol	0.32	231	135	27.4	0.60	0.06	0.87	19.0	7.8	0.28	0.15	0.04	0.14	−0.12	0.17
CH15-5			Ol	0.08	163	115	27.1	0.71	0.06	0.87	18.6	8.9	0.21	0.11	0.05	0.12	0.08	0.13
CH15-7			Ol	0.13	186	103	25.8	0.69	0.08	0.78	19.5	9.2	0.17	0.12	−0.12	0.10	−0.19	0.12
CH17-1	**Type II/PO**	**0.5 mm**	Mes + Ol	0.19	1296	112	21.7	2.20	0.11	3.06	20.7	6.5	0.25	0.88	−0.23	0.14	−0.35	0.14
CH17-2			Mes + Ol	0.07	454	163	23.3	1.30	0.10	1.61	20.1	9.1	0.44	0.27	−0.01	0.12	0.12	0.12
CH18-1	**Type I/PO**	**0.7 mm**	Ol	0.03	77	79	26.5	0.18	0.05	0.33	20.8	7.8	0.11	0.03	−0.09	0.20	−0.31	0.16
CH18-2			Fo	0.05	62	67	28.3	0.25	0.06	0.62	18.6	8.7	0.06	0.02	−0.02	0.13	−0.09	0.14
CH20-1	**Type I/PO**	**0.88 mm**	Fo + alt	0.07	399	455	26.46	2.77	0.03	2.27	18.30	4.98	1.06	0.34	0.18	0.16	0.02	0.14
CH20-2			Fo	0.25	bdl	1	33.07	0.53	0.06	0.20	20.23	0.46	bdl	0.01	0.23	0.12	0.11	0.14
CH20-3			Fo + alt	0.09	bdl	43	31.16	1.00	0.03	0.58	19.59	2.81	0.05	0.01	0.16	0.12	0.14	0.14
CH21-1	**Type I/PO**	**0.86mm**	Ol + Mes	0.11	70	292	12.6	0.99	0.15	2.33	14.6	31.0	0.44	0.08	−0.28	0.11	−0.54	0.10
CH21-2			Fo + Ol	0.29	502	78	26.2	1.36	0.06	1.18	20.8	5.2	0.16	0.35	−0.07	0.14	−0.05	0.12
CH21-3			Fo	0.36	62	122	31.5	0.40	0.03	0.43	19.9	2.5	0.13	0.05	0.01	0.14	0.06	0.15
CH21-4			Fo + Mes + Ol	0.19	798	142	22.9	1.00	0.08	1.96	18.7	11.5	0.23	0.62	−0.05	0.10	−0.13	0.11

CH1-1	**Type II/POP**	**~2 mm**	Ol + Mes	0.15	1040	388	11.4	0.95	0.14	4.55	15.6	26.2	1.18	0.75	−0.21	0.11	−0.53	0.11
CH1-2			Ol +Mes	0.4	1115	333	14.0	1.83	0.10	6.69	22.1	6.6	1.03	2.38	−0.23	0.10	−0.44	0.11
CH1-6			Ol + Mes	0.48	995	331	10.6	1.54	0.12	5.55	17.0	21.6	1.23	1.13	−0.25	0.09	−0.38	0.11
CH1-7			Mes	0.4	1084	296	9.8	2.44	0.12	9.75	19.3	9.5	1.09	4.06	−0.16	0.09	−0.37	0.09
CH1-8			Ol + Mes	0.28	83	206	11.3	3.27	0.16	1.31	17.1	28.0	0.45	0.05	−0.37	0.09	−0.60	0.10
CH6-1	**Type II/POP**	**1.5 mm**	Ol + Mes	0.27	176	260	13.7	1.20	0.12	1.97	17.5	24.9	0.53	0.14	−0.16	0.15	−0.26	0.14
CH6-2			Fo + Ol + Mes	0.6	84	178	17.5	2.36	0.11	2.07	21.2	12.4	0.45	0.26	−0.16	0.19	−0.37	0.13
CH6-3			Px	0.43	82	131	20.7	1.42	0.09	0.90	24.3	6.7	0.36	0.05	−0.15	0.18	−0.48	0.13
CH6-4			Ol	0.02	69	353	12.1	1.28	0.17	1.34	15.1	31.8	1.04	0.05	−0.35	0.18	−0.71	0.12
CH6-5			Ol	0.05	85	312	11.2	1.44	0.15	1.33	15.5	32.4	0.83	0.05	−0.33	0.19	−0.73	0.12
CH6-6			Fo + Mes + Ol	0.48	277	262	19.1	1.58	0.10	1.82	23.9	7.2	0.83	0.18	−0.12	0.15	−0.36	0.12
CH6-7			ol + alt vn	0.17	359	339	11.3	1.52	0.13	2.97	15.5	28.9	0.84	0.27	−0.27	0.19	−0.50	0.13
CH9-4	**Type II/POP**	**2.0 mm**	Fo + Ol + Mes	0.71	bdl	81	22.2	3.08	0.09	3.05	21.0	5.4	0.09	0.08	0.04	0.10	0.03	0.09
CH9-5			Fo + Ol + Mes	0.74	52	122	20.6	2.67	0.10	2.84	20.6	8.7	0.12	0.07	−0.22	0.10	−0.45	0.10
CH9-6			Fo + Ol +Mes	0.28	339	99	17.8	2.27	0.11	3.37	20.3	12.3	0.10	0.24	−0.08	0.12	−0.30	0.10
CH9-7			Ol	0.15	71	557	9.6	0.52	0.13	1.13	13.8	38.5	0.58	0.03	−0.31	0.11	−0.70	0.10
CH9-8			Ol	0.16	85	365	10.6	1.99	0.17	1.61	15.6	32.2	0.53	0.05	−0.35	0.09	−0.73	0.10
CH9-9			Mes	0.19	1641	166	10.8	4.75	0.11	5.68	20.2	13.2	0.27	1.54	−0.27	0.13	−0.43	0.10
CH12-2	**Type II/POP**	**3 mm**	Fo	0.33	183	136	23.4	0.57	0.07	0.99	18.1	14.6	0.18	0.03	0.07	0.15	0.22	0.15
CH12-3			Fo	1.09	bdl	69	29.9	0.39	0.04	0.59	18.5	6.5	0.10	0.06	0.13	0.17	0.21	0.18
CH12-5			Ol	0.1	73	279	10.8	0.21	0.17	1.38	14.9	35.3	0.45	0.04	−0.36	0.14	−0.72	0.16
CH12-7			Mes + alt	0.6	740	145	18.4	4.42	0.08	3.65	19.7	9.2	0.61	0.34	−0.62	0.15	−1.28	0.19
CH12-8			Fo + Ol	0.32	126	307	16.6	1.69	0.08	2.17	15.8	22.5	0.68	0.08	−0.36	0.17	−0.64	0.15
CH14-1	**Type II/POP**	**1.5 mm**	Fo + Mes + alt	0.29	530	253	16.1	1.93	0.12	2.86	20.1	15.5	0.54	0.27	−0.39	0.12	−0.82	0.13
CH14-2			Fo + Mes + alt	0.63	211	125	17.0	3.23	0.09	4.46	20.4	10.6	0.16	0.38	−0.21	0.11	−0.42	0.14
CH14-3			Ol	0.1	101	269	12.4	0.55	0.12	0.86	16.2	31.3	0.41	0.03	−0.35	0.10	−0.75	0.11
CH14-4			Ol	0.15	48	239	14.5	0.69	0.13	1.01	17.5	26.3	0.30	0.03	−0.35	0.10	−0.78	0.13
CH19-1	**Type II/POP**	**0.75 mm**	Ol + Mes	0.25	194	142	17.0	1.61	0.42	1.70	23.4	10.5	0.60	0.08	−0.24	0.13	−0.36	0.10
CH19-2			Ol + Mes	0.18	144	92	17.5	1.34	0.40	1.26	24.3	9.6	0.36	0.07	−0.20	0.12	−0.49	0.10

Sizes of BO chondrules (Ch#2, Ch#8 and CH#11) and CTC (CH#13) analyzed in this study range from 1.0 to 1.4 mm (Table 1). The chondrule textures vary slightly among one another (Fig. 1 and Supplementary Fig. EA1). Major minerals of BO chondrules are forsterite (Mg # 95–99), diopside and anorthite (see Supplementary Table EA1). Mesostasis in Ch#2, Ch#8 and CH#11 shows basic compositions (SiO_2: 47.6–50.4%, Al_2O_3: 16.0–25.0%, MgO: 3.3–8.2%, CaO: 17.6–21.2%), with very low FeO contents (0.34–0.65%). Alteration veins are visible near the rims of Ch#2 and CH#11 (olivine composition is Fe-rich (Mg # 21–42) near the rim and alteration regions). The CTC (CH#13) analyzed in this study has a 250 μm wide porphyritic rim of mainly Fe-rich olivine (Mg # 53) with a barred core (~920 μm diameter) of Mg-rich olivine (Mg # 86–94), anorthite and dispersed Fe-Ni metal grains (sizes range from few μm to 30 μm) (Fig. 1). The radial pyroxene chondrule CH#3 (Fig. 1f) is mainly composed of Ca-Al bearing pyroxene (Supplementary Table EA1).

2.2.2. Porphyritic chondrules

Porphyritic chondrules (PC) are classified as type I and type II based on the average Mg/Fe ratios of their major minerals (classification schemes from McSween, 1977). Type I PC are further classified as porphyritic olivine pyroxene (POP, CH#4, CH#5), porphyritic olivine (PO: CH#7, CH#15, CH#18 and CH#21) and porphyritic pyroxene (PP: CH#10) depending on the occurrence of major mineral phases. Note that this classification could be systematically biased, depending on the mineralogy of the exposed cross-section in 2D, which might be different in 3D (Barosch et al., 2020). However, for this study we are focused on the mineralogical variations in chondrule silicates, therefore reporting the major mineralogy of chondrules in 2D would help in interpretation of the data.

The texture of CH#15 suggests that it is either a highly deformed single chondrule or a mixture of two different chondrules with similar texture and chemical compositions (Fig. 2g). Type I PC mainly consist of Mg-rich olivine (Mg # 82–99), enstatite (En_{88-97}) and minor Fe-rich olivine (Mg # 28–82) near to the rim. The CH#20 (Fig. 2c) is mainly composed of Mg-rich olivine (Mg # 95–99) and Ca-Al bearing pyroxene at the center and Fe-rich olivine (Mg# 28) occurs as an alteration product in the veins. Chondrule CH#21 has a ~ 200 μm thick rim of Fe-rich olivine (Mg

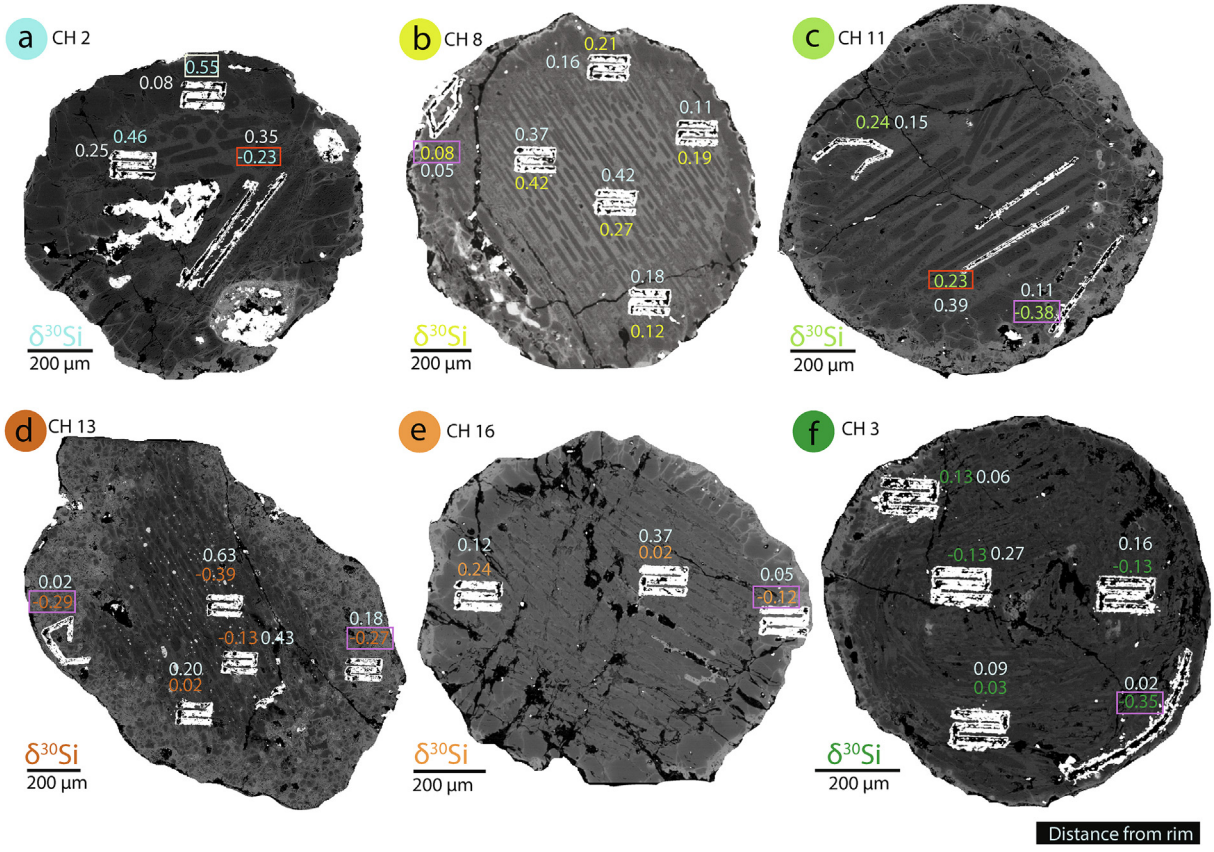

Fig. 1. Backscattered electron images of non-porphyritic chondrules after Si isotope analysis. White color of the laser spots, cracks and holes are due to the leftover of gold coating. δ^{30}Si of each chondrule is shown by a different color, to match the data in the following figures. Light blue colored values near the laser ablation spots correspond to the distance from rim to core. The boxes around the δ^{30}Si values for identification of the major analysed phase are such that yellow box = forsterite, red = mesostasis, and pink = rim. For interpretation of the references to colour in this figure legend, the reader is referred to the web version of this article.

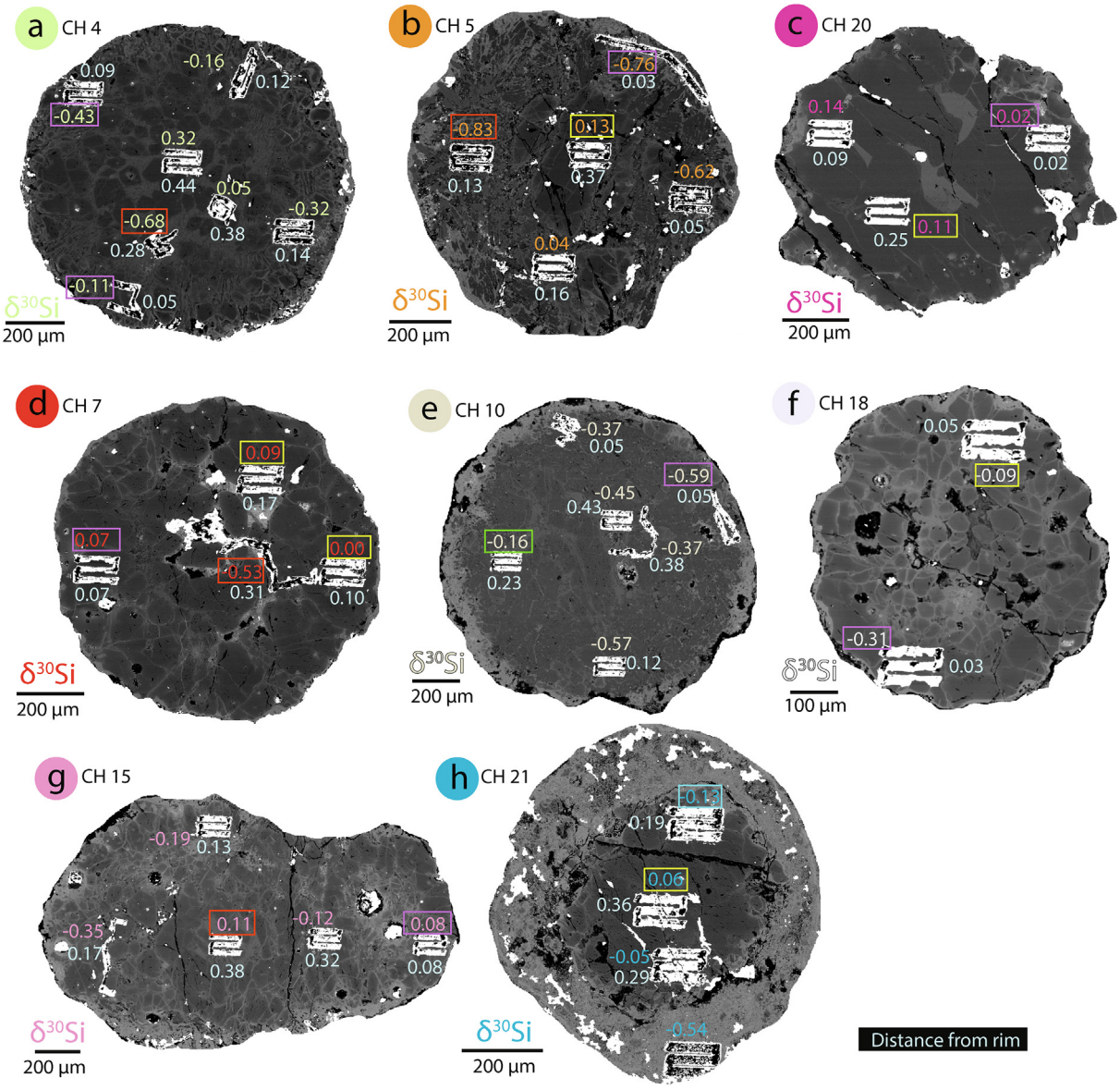

Fig. 2. Backscattered electron images of porphyritic type I chondrules after Si isotope analysis. Laser spots are shown in white color. Similar to Fig. 1, δ^{30}Si of each chondrule is shown by a different color, to match with the data in following figures and light blue colored values near the laser ablation spots correspond to the distance from rim to core. The boxes around the δ^{30}Si values for identification of the major analysed phase are such that yellow box = forsterite, red = mesostasis, green = pyroxene, and pink = rim. (For interpretation of the references to colour in this figure legend, the reader is referred to the web version of this article.)

28). Type I porphyritic chondrules are shown in Fig. 2 and Supplementary Fig. EA2.

Type II chondrules show POP textures (Fig. 3 and Supplementary Fig. EA3, CH#17 and CH#19). Major phases of type II PC consist of olivine (Mg # 26–95) and Fe-bearing orthopyroxene (Mg # 75). Highly altered and opaque mineral-bearing chondrules (CH#1, CH#9, CH#6, CH#12, CH#14) show POP textures ((Fig. 3 and Supplementary Fig. EA3). Highly altered and opaque mineral bearing chondrules are grouped with type II chondrules, because of the similar characteristics of silicate minerology and low Mg/Fe ratio in most phases. Major phases of opaque mineral bearing chondrules consist of olivine (Mg # 26–95), forsterite (Mg # 95–99), orthopyroxene (Mg # 73–98), and high-Ca pyroxene, as well as magnetite and troilite.

2.3. Methods and Mass spectrometry

A petrographic overview of the chondrule types before laser ablation is shown in Supplementary Figs. EA1, EA2 and EA3. Chemical compositions (Supplementary Tables EA1 and EA2) and backscattered electron (BSE) images of selected chondrules were obtained on a JEOL JXA

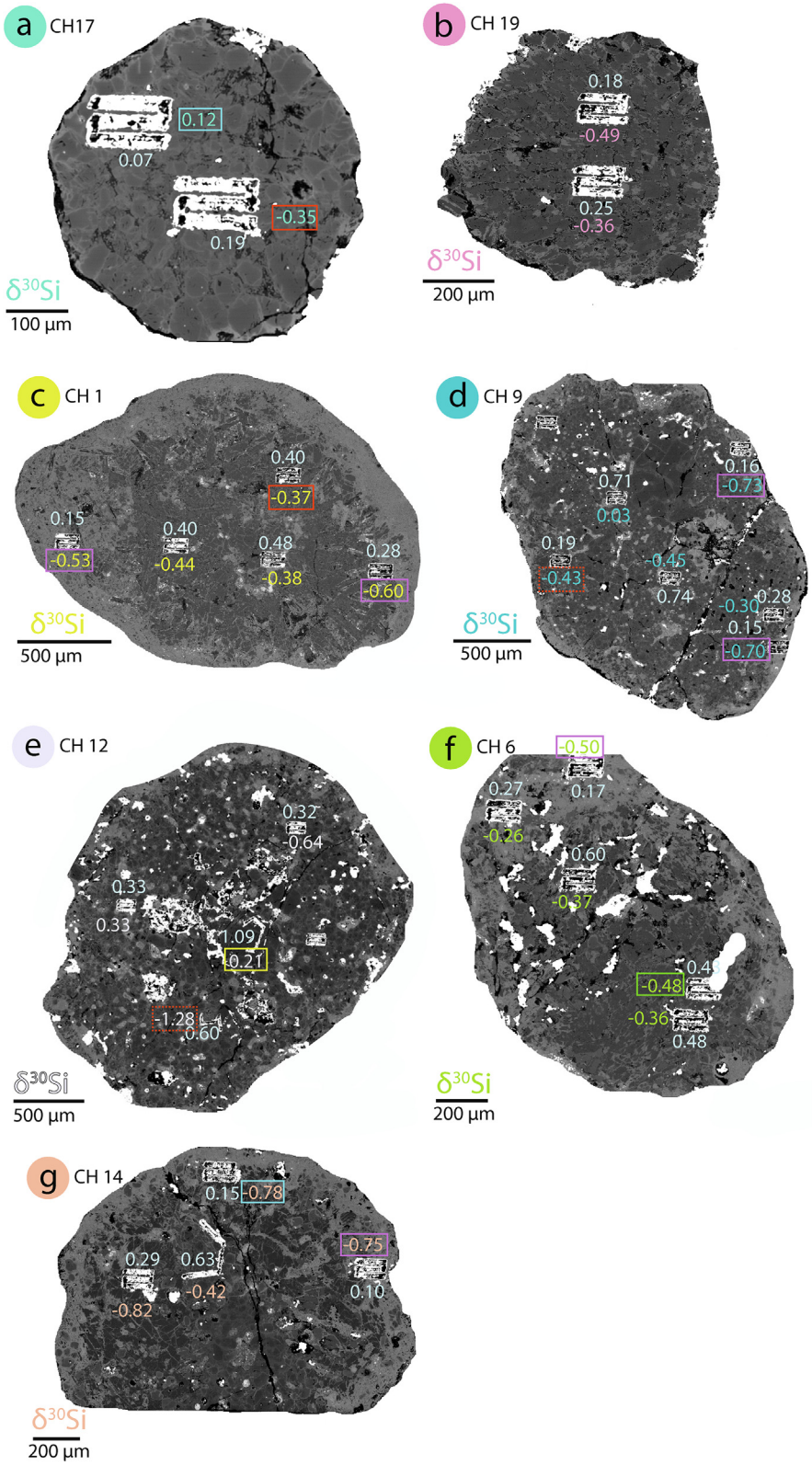

Fig. 3. Backscattered electron images of type II and opaque mineral-bearing porphyritic chondrules after Si isotope analysis. Laser spots are shown in white color. Similar to Fig. 1, δ^{30}Si of each chondrule is shown by a different color, to match with the data in following figures and light blue colored values near the laser ablation spots correspond to the distance from rim to core. The boxes around the δ^{30}Si values for identification of the major analysed phase are such as, yellow box = forsterite, red = mesostasis, green = pyroxene, and pink = rim. Dashed red color boxes are for mesostasis-rich mix analyses. (For interpretation of the references to colour in this figure legend, the reader is referred to the web version of this article.)

8200 Superprobe at Freie Universität Berlin (beam current = 2 nA, accelerating voltage = 15 kV). Backscattered electron images of the analyzed laser spots in chondrule silicates were obtained on a JEOL JSM-6510 scanning electron microscope at University of Potsdam and shown in Figs. 1–3 along with the δ^{30}Si and rim to core distance.

Major, minor and trace element abundances and Si isotope ratios of chondrules were determined *in situ* using femtosecond laser ablation split-stream, combining multi-collector inductively coupled plasma mass spectrometry (LA-MC-ICP-MS; on a Thermo Fisher Scientific Neptune Plus) and quadrupole ICP-MS (on a Thermo Fisher Scientific iCAP) for Si isotope analysis and for element concentration measurements, respectively. Details of the experimental protocols are reported in earlier publications (Schuessler and Blanckenburg, 2014, Frick et al., 2016, Kadlag et al., 2019a). Total raster area of one laser ablated spot is ~ 100 μm × 100 μm. Sometimes to avoid cracks and to analyze pure phases, the lines or irregular shapes are used instead of rectangular raster of the laser beam. Larger raster areas resulted in an analysis of 1–2 different phases in some cases, which can be identified by the comparison of their major element composition with EPMA data (Tables 1 and 2 and Supplementary Table EA1 and EA2). Intensities of ^{28}Si, ^{29}Si and ^{30}Si were measured with a mass resolving power m/Δm > 5000 in medium resolution clipped ion beam mode. Erosion of the entrance slit by the ion beam can lead to a loss of mass resolution with time and thus interference by $^{14}N^{16}O$ on ^{30}Si, resulting in too high δ^{30}Si values. This bias is reflected in deviations from the proportionality of δ^{30}Si and δ^{29}Si outside the analytical precision and quantified by Δ^{29}Si (=δ^{29}Si-0.518 × δ^{30}Si), the isotopic difference from the equilibrium mass fractionation line (originating in the isotope ratios of the bracketing standard). Data in Tables 1 and 2 all reflect analyses with Δ^{29}Si = 0 ± 0.23‰. Silicon isotope ratios of chondrule silicate phases were normalized relative to NBS 28 quartz, which shows a long-term reproducibility of < 0.23‰ δ^{30}Si (2 SE) using the experimental setup described above. Reproducibility and drift in element concentrations and Si isotope ratios were monitored using the reference materials BHVO-2G, NIST610, GOR-132G and ML3B. For two analytical sessions, average δ^{30}Si values of BHVO-2G (synthetic basaltic glass), NIST-610 (synthetic glass), GOR-132G (komatiite) and ML3B (basalt) were −0.34 ± 0.28‰ (2sd, n = 26), 0.12 ± 0.25‰ (2sd, n = 14), −0.22 ± 0.01‰ (2sd, n = 2), and −0.39 ± 0.23‰ (2sd, n = 4) respectively, which is in good agreement with literature data (Armytage et al., 2011, Savage et al., 2010, Zambardi and Poitrasson, 2010, Fitoussi et al., 2009, Schuessler and Blanckenburg, 2014, Tatzel et al. 2015, Frick et al., 2016, Kadlag et al., 2019a).

Major (Mg, Fe, Si), minor (Na, Al, Ca, K), trace lithophile (P, Rb and REE) and siderophile (Pt, Ni, Co, Pd, Au, Ga, Ge and Zn) element abundances were quantified by 100 wt-% oxide normalization. Precision and accuracy of mass fraction determinations were monitored by determining element abundances in well characterized reference materials such as BHVO-2G and GOR-132G calibrated against NIST610 (Jochum et al., 2011). The typical reproducibility of the literature values of major- and trace element concentrations of the reference materials was < 10 % (1 s) (Jochum et al., 2005).

3. RESULTS

The δ^{30}Si values, major, minor and trace element concentration data of chondrule silicates (pure phases as well as mixed analyses) are shown in Tables 1 and 2. Porphyritic and non-porphyritic chondrules analyzed in this study are of variable sizes, with a diameter ranging from 0.5 to 3 mm (Tables 1 and 2). The δ^{30}Si values of chondrules and variation of δ^{30}Si values with major element ratios are presented in Figs. 4 and 5, respectively. CI normalized rare earth elements (REE), Al, and Mg abundance patterns of representative mesostasis analyses are shown in Fig. 6. Abundance patterns of REE, Al, Mg and siderophile elements normalized to CI chondrites for analyzed silicates are given in the Supplementary Figs. EA4, EA5 and EA6.

3.1. Non-porphyritic chondrules

Barred olivine chondrules are mainly comprised of forsterite and Aluminum-rich mesostasis (Fig. 1, Supplementary Table EA1). δ^{30}Si values of ablated BOC silicate phases range from −0.38 ± 0.18 (all reported uncertainties on δ^{30}Si are 2 SE)‰ to 0.55 ± 0.20‰ (Table 1, Fig. 4). The highest δ^{30}Si value (0.55 ± 0.20‰) occurs in a forsterite-rich olivine (Mg # 94) in a BOC CH#2 (Table 1, Fig. 4) and lowest δ^{30}Si is observed in the analysis at the rim from BOC CH#11 (Figs. 1 and 4).

Iron-poor phases of BOC (forsterite + mesostasis) have higher δ^{30}Si values compared to Fe-rich phases (alteration veins and olivine rims (Mg# 42–90). REE concentrations in mesostasis of BOC are ~ 10 to 20 × CI chondrites (Fig. 6a, b, c), whereas olivine-rich and mixed analyses show REE concentrations of up to 2 to 8 × CI chondrites and in some cases, Sm, Eu and Tm abundances below the detection limit (Supplementary Fig. EA4, EA5 and EA6 and Supplementary Table EA3). Negative correlations between δ^{30}Si and Ca/Na are observed in BOC CH#2 (Fig. 5e).

The δ^{30}Si values of CTC (CH#13) range from −0.39 ± 0.17‰ to 0.02 ± 0.14‰ (Table 1, Fig. 4). δ^{30}Si values of RP range from −0.35 ± 0.16‰ to 0.13 ± 0.16‰. Mg/Fe and Mg/Si range from 0.80 to 16.9 and from 0.62 to 1.42, respectively. In CTC, the REE concentrations in the mesostasis are similar to the mesostasis in BOC, but show depletions in Eu and Tm (Fig. 6a); other analyses show REE concentrations from 1 to 4 × CI chondrites and concentrations of Sm, Eu, Tm and Lu below detection limit in some cases (Supplementary Fig. EA4).

The δ^{30}Si values of RPC show no systematic variation with Mg/Fe or Mg/Si, however, δ^{30}Si values of RPC show an inverse relationship with the Ca/Na ratio (Fig. 5e). In case of RPC, REE concentrations (Supplementary Fig. EA4) in mesostasis-rich analyses are higher than in CI chondrites (3 to 8 × CI). In most cases, the siderophile element abundances (Supplementary Fig. EA4) are less than in CI chondrites (1 to 0.01 × CI).

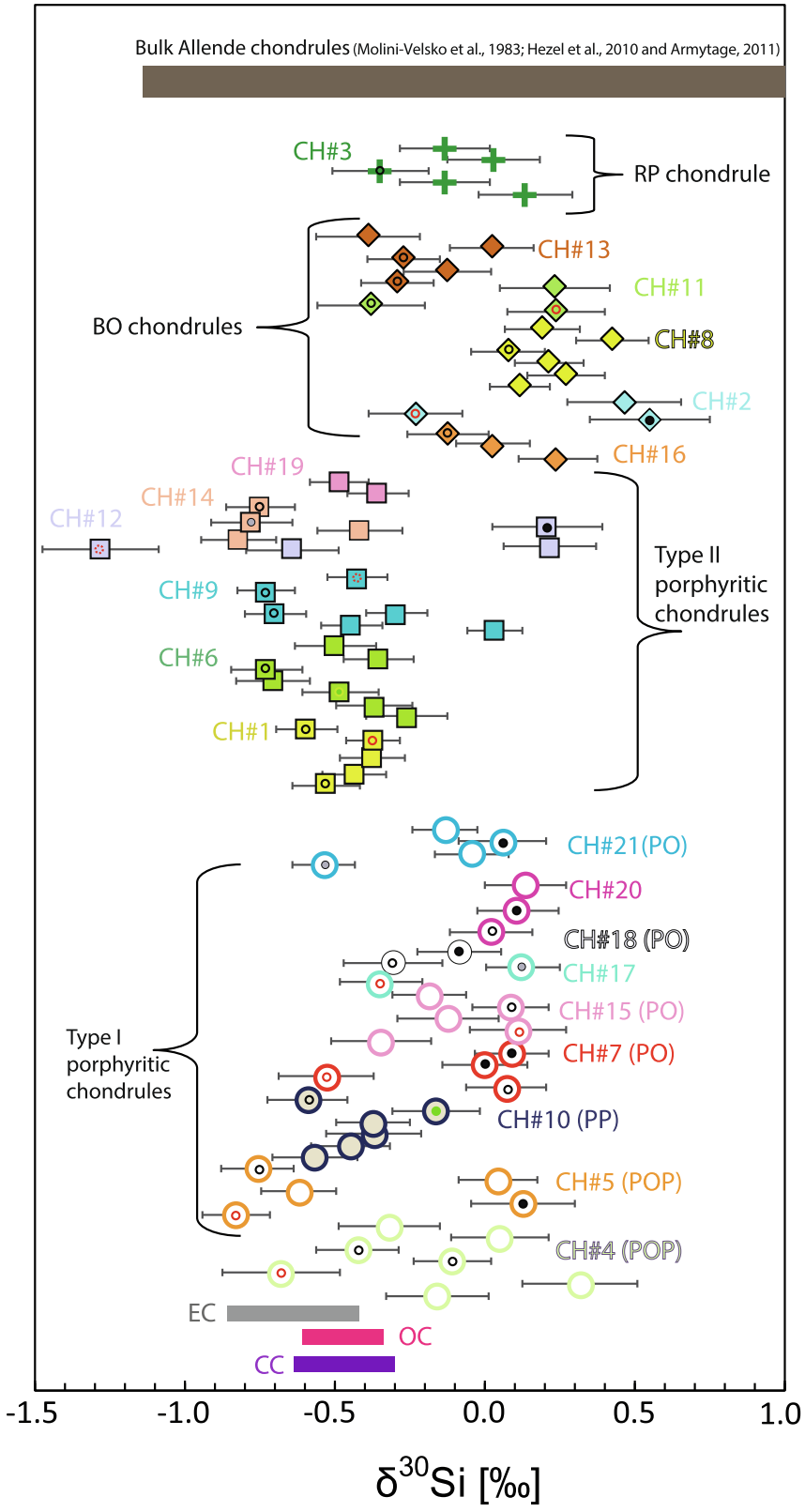

Fig. 4. δ^{30}Si values of chondrule silicates analyzed in this study. The range of literature δ^{30}Si values of bulk carbonaceous chondrites, ordinary chondrites, enstatite chondrites and individual chondrules from the Allende meteorite is shown for comparison (Molini-Velsko et al., 1983; Georg et al., 2007; Fitoussi et al., 2009; Chakrabarti and Jacobsen, 2010; Hezel et al., 2010; Armytage 2011; Armytage et al., 2011; Savage and Moynier, 2013). Red open circle = mesostasis, red dotted circle = mesostasis-rich, black solid circle = forsterite, black open circle = analysis from rim, green solid circle (yellow border in CH#6) = pyroxene, and grey solid circle = Fe-rich olivine. (For interpretation of the references to colour in this figure legend, the reader is referred to the web version of this article.)

3.2. Porphyritic chondrules

The Fe-Ni metal-bearing and highly altered chondrules (CH#1, CH#6, CH#9, CH#12, CH#13, CH#15) are slightly more deformed in shape compared to metal-poor chondrules (type I and type II chondrules) and also comparatively larger in size (Figs. 1–3). The δ^{30}Si of type I PC range from -0.83 ± 0.11‰ to 0.32 ± 0.19‰. Most analyses from type I POC show high δ^{30}Si values (ranges from -0.54 ± 0.10‰ to 0.12 ± 0.12‰), type I POPC show higher as well as lower values (ranges from -0.83 ± 0.11‰ to 0.32 ± 0.19‰), and type I PPC shows intermediate values (ranges -0.59 ± 0.13‰ to -0.16 ± 0.15‰) (Fig. 4). The δ^{30}Si of type II PC from -0.49 ± 0.10‰ to 0.12 ± 0.12‰, respectively (Table 2, Fig. 4). Highly altered and opaque mineral bearing chondrules show variation in the δ^{30}Si from -1.28 ± 0.19‰ to 0.24 ± 0.13‰. The largest chondrule (CH#12, 3 mm diameter) shows large variations in δ^{30}Si of up to 1.5‰ between different minerals.

The raster analyses from porphyritic chondrules show systematic variations of δ^{30}Si (Fig. 5). Mg-rich compositions of all analysed spots from PC are systematically higher in δ^{30}Si than Fe-rich or Ca, Al-rich compositions (in case of pyroxene) in the same chondrule (Table 2). A systematically larger spread of δ^{30}Si is observed in type I POPC compared to type I POC and PPC (Fig. 4).

The Mg/Fe and Mg/Si ratios in analyzed spots in porphyritic chondrules range from 0.25 to 18.31 and from 0.51 to 1.62, respectively. The δ^{30}Si in different analyses of type I PC are variable and independent of Mg/Fe (Fig. 5b). In porphyritic chondrules, the concentrations range from 1 to 10 × CI chondrites for most REEs in case of mesostasis-rich spots (Fig. 6 and Supplementary Figs. EA5 and EA6). The siderophile element abundances (Supplementary Figs. EA5 and EA6) range from 4 to 0.01 × CI. Higher abundances of siderophile elements are observed in the opaque mineral bearing chondrules (Supplementary Fig. EA6).

4. DISCUSSION

4.1. δ^{30}Si and the physical and chemical properties of chondrules

No systematic dependence of chondrule sizes and variation of δ^{30}Si was observed in chondrule minerals (Tables 1 and 2). However, the largest chondrule (CH#12) shows the largest variation in inter-mineral δ^{30}Si values (1.5‰). These observations indicate that with increasing chondrule sizes, the interaction of chondrule silicates with surrounding gas and matrix is variable and higher. The δ^{30}Si values of bulk chondrules from Clayton et al. (1983) show a systematic decrease (up to 1‰) with increasing chondrule sizes, which supports this scenario. However, without chemical composition of these chondrules we cannot directly compare if this variation is related to the chondrule sizes or variable chemistry (Mg/Fe) and mineralogy.

The δ^{30}Si values of chondrule phases are not directly dependent on the spatial position (e.g. distance to rim or core) and appear to be more dependent on the Mg/Fe variation of the minerals (Fig. 5). In general, olivines near chondrule rims tend to be Fe-rich (Mg# range 26–90) and lower δ^{30}Si values appear towards chondrule rims (Figs. 1–4). Correlations of δ^{30}Si with Mg/Fe also occur for silicates at larger rim to core distance (e.g. Fig. 3, CH#9, CH#12).

The variation between Mg/Fe, Mg/Si and δ^{30}Si in chondrule silicates shows two behaviors, i) linear correlations between Mg/Si, Mg/Fe and δ^{30}Si and, ii) scattered variation of Mg/Fe and Mg/Si without significant change in the δ^{30}Si (Fig. 5a, 5b, 5c and 5d). The role of nebular alteration and parent body processing for these variations is discussed in the following sections.

4.2. Δ^{30}Si of mineral pairs: equilibrium or non-equilibrium fractionation?

The δ^{30}Si of most BOC, RPC silicates are similar to type I PC, but higher compared to type II POC, POPC and PPC (Fig. 4). The δ^{30}Si values of most analyses in the BOC CH#8 and CH#11 are similar, because all of these are mixed analyses of forsterite and the mesostasis. In contrast, there is an up to 0.78‰ difference in δ^{30}Si between analysis areas with a high mesostasis fraction and those with a high forsterite fraction in CH#2 (Table 1). The variation of δ^{30}Si of up to 0.46‰ between the mesostasis of CH#11 and CH#2 (Table 1, Figs. 1 and 4) indicates different formation histories of different BOC chondrules from the same meteorite.

Equilibrium or non-equilibrium isotope fractionation can be inferred from the inter-mineral variation of δ^{30}Si. In CH#2 (BOC), $\Delta^{30}Si_{mesostasis\text{-}olivine}$ is −0.78 (Table 1), which is similar to the $\Delta^{30}Si_{pyroxene\text{-}olivine}$ in type I POP chondrules CH#4 and CH#5 (−0.73 and −0.75 respectively, Table 2). The theoretical high temperature ($T > 1200$ K) equilibrium Si isotope fractionation between orthopyroxene and olivine or feldspar and olivine is < 0.1‰ (Méheut et al., 2009; Huang et al., 2014; Méheut and Schauble, 2014; Qin et al., 2016). Therefore, higher $\Delta^{30}Si_{olivine\text{-}pyroxene}$ and $\Delta^{30}Si_{olivine\text{-}mesostasis}$ values associated with olivine, orthopyroxene and mesostasis cannot reflect equilibrium isotope fractionation at high temperatures.

High cooling rates might have prevented equilibration of Si isotopes in heterogeneous domains of CH#2. However, the abundances of REE and siderophile elements in mesostasis and forsterite (Fig. 6, Supplementary Fig. EA4) indicate preferred partitioning of REE into the mesostasis compared to forsterite, which is expected from the equilibrium partitioning of these elements between melt and olivine (Nielsen et al., 1992). Also, the abundance pattern of Ni, Co and Fe are similar in forsterite and mesostasis (Supplementary Fig. EA4). Therefore, the differences in δ^{30}Si between mesostasis and forsterite may reflect their different susceptibilities to chemical and isotopic exchange with the nebular gas.

Forsterite-rich olivine is present in the rim and mantle of CH#2, where its coarse grain size may have limited the chemical and isotope exchange with the surrounding gas. Mesostasis on the other hand is porous (Fig. 1 and supplementary Fig. EA1) and therefore more easily affected by alteration in the solar nebula as well as on the meteorite

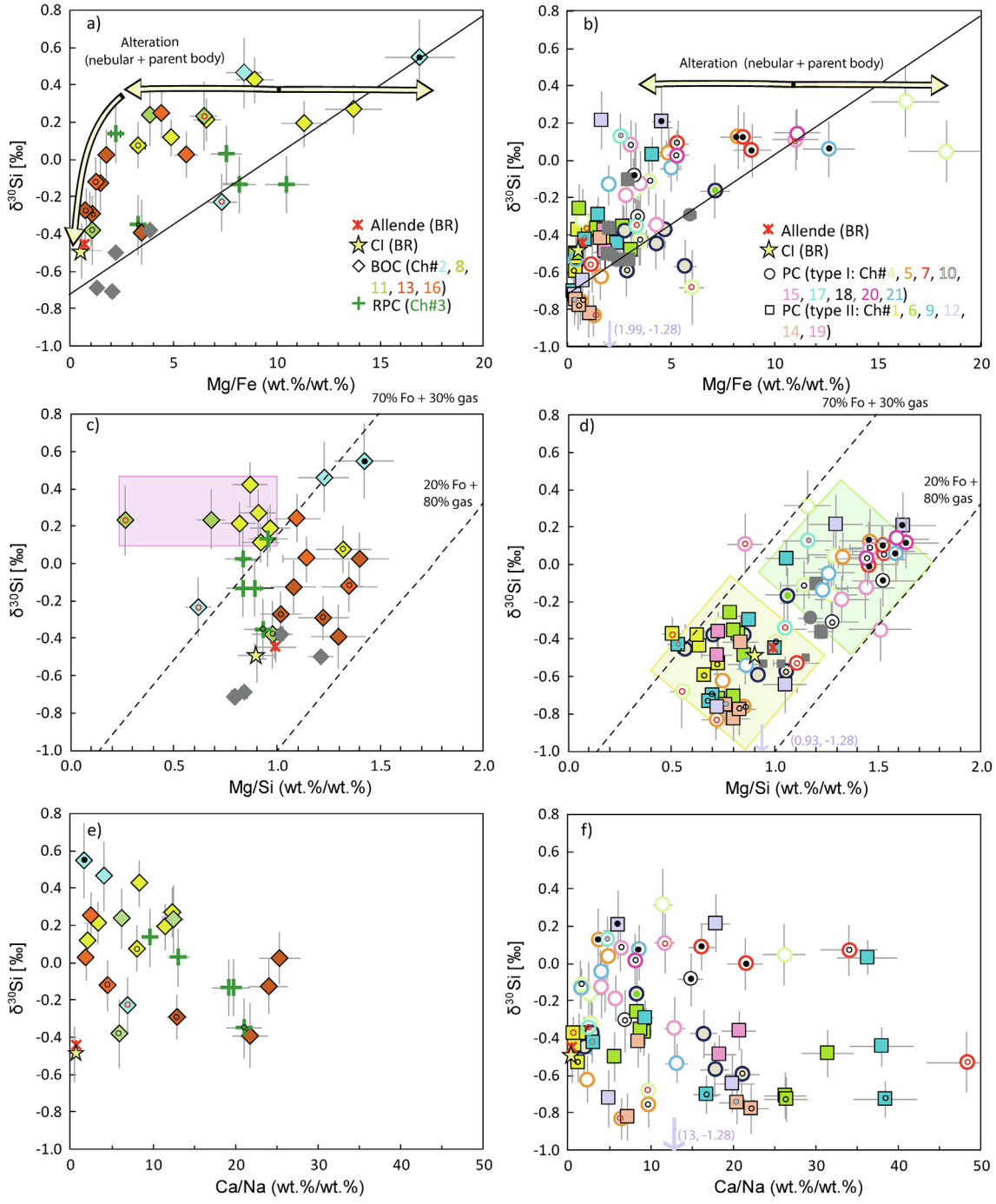

Fig. 5. δ^{30}Si versus major element ratios (wt.%/wt.%) in chondrules from the Allende meteorite (a-c: non-porphyritic chondrules, d-f: porphyritic chondrules). (a, b) δ^{30}Si *vs.* Mg/Fe; (c, d) δ^{30}Si *vs.* Mg/Si; (e, f) δ^{30}Si *vs.* Ca/Na. The δ^{30}Si and major element data for bulk Allende and CI chondrites is from (Jarosewich et al., 1987; Lodders, 2003; Georg et al., 2007; Fitoussi et al., 2009; Armytage et al., 2011; Zambardi et al., 2013). Gray symbols are bulk chondrule data for Allende chondrules from Armytage (2011). Chondrule analyses show no systematic variation in δ^{30}Si *vs.* Ca/Na, except for the radial pyroxene chondrule (RPC). RPC show an inverse correlation between δ^{30}Si *vs.* Ca/Na. δ^{30}Si correlates with Mg/Fe (black correlation line). Correlated variations between δ^{30}Si and Mg/Si occur in most porphyritic chondrules (c and d). Non-porphyritic chondrules have higher average δ^{30}Si values than CI chondrites and show significant variations in the Mg/Si ratio. This difference can be explained by the variable relative contributions of kinetic and equilibrium isotope fractionation processes in texturally different chondrules. If the δ^{30}Si and Mg/Si values of the chondrule minerals resulted from the equilibrium fractionation of early formed solids and remaining nebular gas with CI chondrite-like initial composition, they would fall between the two dashed lines in Figs. (c) and (d). This area represents the window of solid–gas equilibrium isotope fractionation and interaction of 70% to 20% of forsterite with 30% to 80% remaining SiO_{gas}. Details of the calculations are provided in the Supplementary Information. The two solid lines represent the window of kinetic isotope fractionation between 50% solid and 50% gas (line towards higher Mg/Si) and 20% solid and 80% gas (towards lower Mg/Si). The variation of δ^{30}Si and Mg/Si in all porphyritic chondrules and in some non-porphyritic chondrules reflects equilibrium isotope fractionation between early-crystallized silicates (mainly forsterite) and nebular gas (SiO_{gas}). Non-systematic variations of δ^{30}Si and Mg/Si in barred olivine chondrules that fall into the pink field reflect kinetic isotope fractionation during the formation of these chondrules.

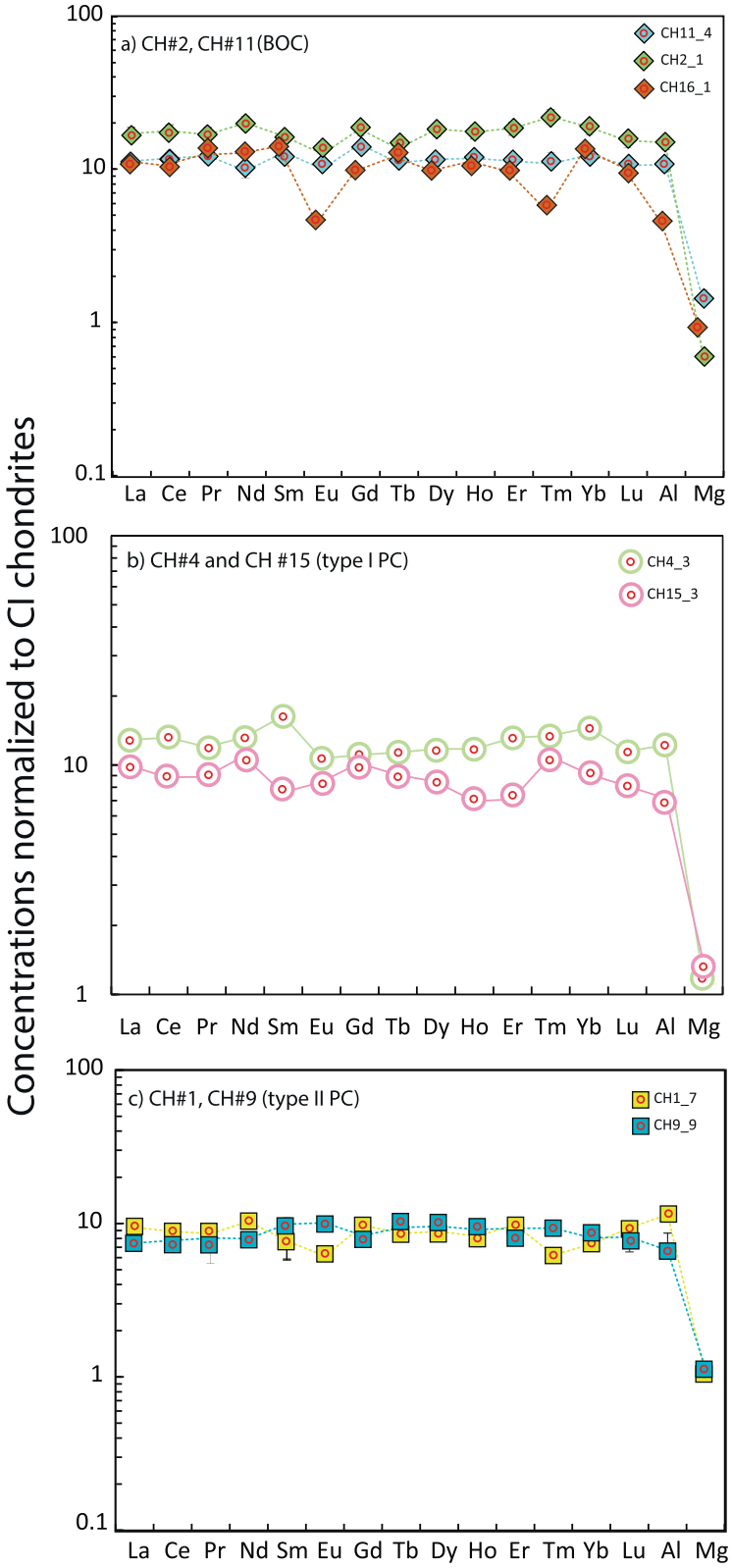

Fig. 6. CI chondrite-normalized REE, Al and Mg abundance patterns of mesostasis in (a) non-porphyritic chondrules, (b) porphyritic (type I) chondrules, and (c) porphyritic (type II) chondrules from the Allende meteorite. CI chondrite values are from Lodders (2003). REE in mesostasis from all types of chondrules are 10–20 times enriched compared to CI chondrites and are mostly unfractionated.

parent body (Lewis and Jones, 2019). If higher δ^{30}Si of the early-formed forsterite is an effect of equilibrium condensation between solid and gas (Dauphas et al., 2015), then the lower δ^{30}Si of the mesostasis may have been caused by interaction with SiO from nebular gas with low δ^{30}Si during the formation of mesostasis (see Supplementary Information for details). Parent body alteration is unlikely to have caused the difference in δ^{30}Si between forsterite and mesostasis of CH#2, because alteration veins at the rim of this chondrule are rich in Fe (Housley and Cirlin, 1983), whereas Fe enrichment is not observed in the mesostasis (Tables 2 and 3). Therefore, the combination of solid-melt-gas equilibrium and kinetic isotope fractionation during chondrule formation is necessary to explain the observed variation between forsterite and mesostasis of BOC.

The observed variation of δ^{30}Si with chondrule mineralogy in porphyritic chondrules can be explained by variable equilibrium fractionation of Si isotopes between solid and gas (Dauphas et al., 2015). Equilibrium isotope fractionation between solids and gas during condensation and between melt and gas during evaporation leads to early-formed Mg-rich olivine and pyroxene with higher δ^{30}Si and coexisting SiO gas with lower δ^{30}Si relative to the starting composition (Chaussidon et al., 2008; Harju et al., 2015; Krot et al., 2004a; Libourel et al., 2006; Jacquet et al., 2012; Friend et al., 2016). Mg-rich olivines are main nucleation sites for mesostasis and clinopyroxene (Na, Ca and Al-rich analyses, Tables 1 and 2), which continues to react with SiO in nebular gas with low δ^{30}Si after Mg-rich olivine has formed. The oxidation of SiO in the gas phase during cooling results in the formation of SiO_2, which reacts with olivine to form orthopyroxene. The higher fO_2 required for this process is either achieved by vaporization of the dust or by hydrogen loss at high temperatures (Hua et al., 1988). The observed large differences (up to −0.78‰) between olivine and -mesostasis (mainly in type I chondrules) suggest that the nucleation of the mesostasis at the grain boundaries of olivine prevented further interaction of olivine with the ^{30}Si depleted nebular gas. The proposed gas-melt-solid reactions that explain the differences in the O isotope ratios of pyroxene and olivine (Chaussidon et al., 2008) are:

$$SiO_{(gas)} + 12\ x\ O_{2(gas)} = SiO_{2(melt)} \quad (1)$$

$$Mg_2SiO_{4(olivine)} + SiO_{2(melt)} = Mg_2Si_2O_{6(pyroxene)} \quad (2)$$

These reactions should also affect Si isotopes, where half of the Si in pyroxene is derived from the olivine precursor and the other half from $SiO_{(gas)}$. Using isotope mass balance, $\delta^{30}Si_{SiO(gas)}$ values can be calculated from the equation $\delta^{30}Si_{SiO(gas)} = (2x\delta^{30}Si_{pyroxene\ or\ mesostasis} - \delta^{30}Si_{olivine})$. According to the $\Delta^{30}Si_{pyroxene\text{-}olivine}$ and $\Delta^{30}Si_{mesostasis\text{-}olivine}$ values observed in chondrules (−0.75 and −0.78, respectively), the δ^{30}Si of the $SiO_{(gas)}$ must have been ~−1.4‰ during the formation of pyroxene in type 1 POP chondrules (CH#4 and CH#5) and ~−1.0‰ during the formation of mesostasis in BOC CH#2. If the starting average δ^{30}Si value of nebular gas was CI chondrite-like ($\delta^{30}Si_{CI}$ = -0.48‰) and if Mg-rich olivine ($\delta^{30}Si_{Forsterite}$ = 0.55‰) formed under equilibrium conditions, then the remaining nebular gas should have δ^{30}Si as low as −1.75‰ (calculated assuming equilibrium fractionation between forsterite and nebular gas is $\Delta^{30}Si_{Forsterite\text{-}SiO(gas)} = 4.2 \times 10^6/T^2$, Méheut et al., 2009; Javoy et al., 2012; Dauphas et al., 2015, for details see Supplementary Information section 1). The pyroxene formed from the interaction of ^{30}Si-depleted gas (i.e. δ^{30}Si = −1.75‰) with olivine under equilibrium conditions should have δ^{30}Si ~ −0.7‰.

We note that δ^{30}Si in the mesostasis of all non-porphyritic chondrules is significantly higher than this value (Table 1). This may be due to partial equilibration of mesostasis and olivine during repetitive evaporation and condensation during gas-chondrule melt interaction. Because of the negligible contributions from equilibrium Si isotope fractionation between the silicate phases at high temperatures (Méheut et al., 2009; Huang et al., 2014; Méheut and Schauble, 2014), the Si isotope systematics of the mesostasis reflect their crystallization and cooling history and their variable interaction with ^{30}Si-depleted gas.

Another important variation observed in the Si isotope composition of chondrule silicates is the systematically lower δ^{30}Si of Fe-rich olivine and pyroxene compared to Mg-rich olivine and pyroxene in the same chondrule (Fig. 5a and 5b). This could be explained by the interaction of Mg-rich phases with cooling nebular gas (low δ^{30}Si) and the late formation of Fe-rich minerals during chondrule crystallization.

Another process which could potentially relevant here is the equilibrium isotope fractionation of Si in minerals that form solid solutions. A preference of ^{30}Si occurs with decreasing Si-O atomic bond length in different polymorphs of Mg_2SiO_4, such as forsterite, wadsleyite and ringwoodite (Huang et al., 2014), confirming the theory that short bonds are relatively stronger and enrich heavy isotopes under equilibrium conditions (Urey, 1947). If this can be extrapolated to the olivine solid solution, then Fe-rich olivine must have lower δ^{30}Si compared to Mg-rich olivine as Si-O bond-lengths of fayalite are longer compared to forsterite (Birle et al., 1968). The data from this study are consistent with this trend. However, at this stage we do not have direct quantitative evidence from theoretical or experimental data to determine effect of this process and also, it is not known if significant fractionation of Si isotopes can occur in different solid solutions of olivine.

A difference of δ^{30}Si of up to 0.9‰ is observed in Fe-rich and Mg-rich olivine analyses in individual porphyritic chondrules (CH#5, CH#7, CH#12, CH#14, CH#21), especially from the rims (Fe-rich) and cores (Mg-rich) of some chondrules (e.g. CH#21). These differences may represent effects of both, the formation of Si- or Fe-rich minerals in the solar nebula (e.g., fayalite or orthopyroxene from ^{30}Si depleted SiO_{gas}) as well as later aqueous alteration (mainly causing Mg/Fe variations) on the Allende parent body. Some analyses from the same chondrule do not follow the correlation of δ^{30}Si with Mg/Fe (as indicated by the yellow arrows in Fig. 5), possibly because of the local mobilization of Fe during parent body alteration (e.g. in CH#7). Earlier studies suggest that Allende is significantly affected by parent body alteration (Krot et al., 1997, 1998). A thick rim

(~100 μm) of Fe-rich olivine around CH#21 shows a low δ^{30}Si value of −0.54 ± 0.10‰ compared to the core that ranges from 0.06 ± 0.15‰ to −0.13 ± 0.11‰. Rubin and Wasson (1987) argued that the thick rims of Allende chondrules were formed from precursors similar to the matrix. If correct, then chondrule rims should have δ^{30}Si similar to the matrix. The mass balance of Mg, Fe and δ^{30}Si of chondrules and bulk rock data of Allende (Jarosewich et al., 1987; Armytage et al., 2011) suggest that the matrix silicates are Fe-rich (low Mg/Fe) and have lower δ^{30}Si values than chondrules. A systematic study of δ^{30}Si in matrix silicates (average $\delta^{30}Si_{matrix} = -0.61 \pm 0.10$, (2SE) and average $Mg/Fe_{matrix} = 0.38 \pm 0.10$ (2sd)) supports this scenario (Kadlag et al., 2019b). Therefore, our data support both hypotheses, that fayalite-rich chondrule rims either formed during open system parent body alteration or from the same material as the matrix in a cooling nebular environment.

The Mg/Fe and δ^{30}Si of most chondrule silicates (Fig. 5a and 5b) are higher than values for bulk Allende (note that the Mg/Fe and δ^{30}Si values in bulk Allende is also similar to CI chondrites) and Allende matrix (Kadlag et al., 2019b). The complementary variations of Si isotopes and major elements in Allende chondrules and matrix suggests the formation of chondrules and matrix from a reservoir in the solar nebula with CI-chondrite like Mg-Fe-Si systematics, consistent with other studies (Chaussidon et al., 2020).

We conclude that the variation of δ^{30}Si in chondrule minerals reflects multi-stage processes. Silicon isotope fractionation during high-temperature processing is most evident in BOC and type I PC and resulted in high δ^{30}Si compared to CI chondrites, whereas lower Mg/Fe and δ^{30}Si in chondrules could have been inherited from nebular and later Mg/Fe fractionation during parent body alteration processes. Matrix formed from remaining nebular gas which has low Mg/Fe and low δ^{30}Si after chondrule formation, consistent with other studies (Chaussidon et. al., 2020). Altered (Fe-rich) chondrule minerals and chondrule rims show Mg/Fe and δ^{30}Si similar to the matrix, which suggests the formation of chondrule rims and Fe-rich phases by interaction of alteration fluids with matrix material.

4.3. Relationship between type I and type II chondrules

4.3.1. Chemical and Si isotopic composition

Several chemical, isotopic, and experimental studies were carried out to understand the relationship between type I and type II chondrules (summarized in Jones et al., 2005; Hewins et al., 2005), however, it is still not clear if and how type I and type II chondrules are related to each other. Some studies suggest that type I chondrules were derived from type II chondrules by evaporation and reduction in the solar nebula (Libourel and Chaussidon, 1995; Sears et al., 1996; Jones and Danielson, 1997; Lemelle et al., 2001; Leroux et al., 2003; Hewins et al., 2005; Jones et al., 2005; Villeneuve et al., 2015). Other studies suggest that type II chondrules derive from oxidation of type I chondrules (Ruzicka et al., 2008; Schrader et al., 2008). Besides Fe content and oxidation state, a major difference between type I and type II chondrules is the enrichment of moderately volatile elements in type II chondrules compared to type I chondrules (Hewins et al., 2005). We scrutinize the compatibility of these two opposing models with our elemental and Si isotope data. If type II chondrules derived from type I chondrules, then Mg in silicates was replaced by Fe to form Fe-rich olivine or Fe-rich pyroxene depending on the availability of O_2 and Fe and SiO_{gas}:

$$MgSiO_3 + Fe + 1/2\ O_2 = MgFeSiO_4 \quad (3)$$

$$Mg_2SiO_4 + 2Fe + 2\ 1/2\ O_2 + 3\ SiO_{gas} = 2MgFeSi_2O_6 \quad (4)$$

The reactions shown in Eqs. (3) and (4) either occur under oxidizing conditions in the solar nebula or during parent body metamorphism (Housley and Cirlin, 1983; Weinbruch et al., 1990; Krot et al., 1997, 1998). During the formation of Fe-rich olivine (Eq. (3)), no Si isotope exchange occurs. The oxygen required in Eq. (3) was either present in the solar nebula under oxidizing conditions (Hua et al., 1988; Weinbruch et al., 1990) or was released during hydrothermal alteration on the parent body (Krot et al., 1997, 1998).

If, Fe-rich enstatite formed from Mg-rich olivine by reaction (4) with isotopically light (low δ^{30}Si) nebular gas (lower δ^{30}Si, because of previous forsterite-gas fractionation, Méheut et al., 2009; Javoy et al., 2012; Dauphas et al., 2015), then the δ^{30}Si of Fe-rich enstatite of type I and type II chondrules should be consistently lower than values in Mg-rich enstatite, which matches the data (RPC CH#3 in Fig. 5a and CH#10 from Fig. 5b). We note that reaction of Mg-rich enstatite with Fe and O_2 (reaction (3)) to form Fe-rich olivine during close system parent body metamorphism cannot be responsible for the systematic depletion of ^{30}Si in Fe-rich olivine from chondrules. Instead, a two-stage process would be required in which precursor enstatite acquired isotopically light Si (for instance by open system isotope exchange with low-δ^{30}Si nebular gas), followed by reaction (3).

In case of the reaction of forsterite and remaining nebular gas to form Fe-rich pyroxene (Eq. (4)), half of the Si in Fe-rich pyroxene is derived from SiO_{gas}. The δ^{30}Si and Mg/Si of chondrule silicates show bimodal distributions in all porphyritic chondrules (yellow and green fields in Fig. 5d). These observations along with variations in Fe content (Fig. 5b) suggests that pyroxenes ($Mg/Si \leq 1$) and Fe-rich olivines ($Mg/Si \leq 1.4$) formed later than Mg-rich olivine ($Mg/Si \geq 1.5$) in the sequence of events. The large spread of δ^{30}Si in Mg-rich olivine (Fig. 5 a and b) suggests heterogeneity in the Si isotope composition of Mg-rich olivines, which may have occurred due to incomplete equilibration with the surrounding gas because of repetitive fast heating and cooling cycles. Overall, these relationships are consistent with the formation of type II chondrules from type I chondrules and alteration of opaque mineral bearing chondrules by open system isotope exchange during nebular and parent body processing.

An alternative view in previous studies is that type I chondrules may have formed from type II chondrules via

reduction of Fe. The reduction of Fe (Hewins et al., 2005) is expressed as

$$Fe_2SiO_4 = 2Fe_{metal} + x\ SiO_{2melt} + (1\text{-}x)\ SiO_{gas} + (3\text{-}x)/2\ O_{2gas} \quad (5)$$

The validity of this scenario and its effect on Si isotopes in chondrule silicates can be studied by comparison of the metal-poor type I (Supplementary Fig. EA2) and opaque mineral-rich type I chondrules (Supplementary Fig. EA3). Most silicates from metal poor type I chondrules (e.g. CH#4, CH#5, CH#7, CH#20) have higher δ^{30}Si (Fig. 4) compared to metal-rich type I chondrules of similar sizes (e.g. CH#1, CH#14). Silicates from type II chondrules (CH#17, CH#19) also show systematically lower δ^{30}Si compared to type I chondrules. Finally, the matrix also shows lower δ^{30}Si compared to most silicates from type I chondrules (Kadlag et al., 2019b; Chaussidon et al., 2020).

Higher δ^{30}Si values of type I chondrules compared to type II chondrules (Fig. 4) might be explained by the release of ^{28}Si-enriched SiO_{gas} via reduction and evaporation process during formation of type I chondrules from type II chondrules. The role of Rayleigh process in this scenario is discussed in detail in Supplementary material section 3 and shown in Fig. EA7). Low dust/gas ratio required for higher evaporative loss of ^{28}Si compared to ^{30}Si during the formation of type I chondrules from type II chondrule precursors, otherwise the Si isotope fractionation is insignificant (Galy et al., 2000; Young et al., 1998; Fig. EA7). This is not consistent with other studies, which shows that the high dust/gas ratio (>50 × solar value) is required during chondrule formation (Galy et al., 2000; Hertwig et al., 2018). In order to preserve matrix dust (the most fragile and oxidized component) the accretion region of the Allende meteorite must have been more oxidized compared to type I chondrules. Then, the latter likely derived from a different, more reduced region of the solar nebula. In such as case, the total variation of δ^{30}Si in chondrules should be much higher than 2‰ due to random sampling of the variably processed unequilibrated solid precursors that formed at different conditions and locations. Similarly, random chemical variations should occur in chondrules and the matrix. The limited variation in δ^{30}Si (this work) and complementary chemical variations in matrix, type II chondrules and type I chondrules (Hezel and Palme, 2010) suggest that all these components of Allende were likely formed in a similar or common reservoir.

The overall systematics is indicative of the oxidation of an earlier, reduced minerology of the Allende meteorite, rather than reduction of an oxidized assemblage. Also, reduction and loss of Fe-metal from chondrule melt (equation (5)) would affect abundances of siderophile elements in chondrules in specific ways, which will be discussed in the next section.

4.3.2. Siderophile element abundances

All chondrules analyzed in this study show lower siderophile element abundances compared to CI chondrites (Supplementary Figs. EA4, EA5 and EA6). Most type I PC and BOC are devoid of Fe metal and show high Mg/Fe, consistent with previous data (Figs. 1 and 2; Hezel and Palme, 2010), whereas the matrix of Allende has lower Mg/Fe and δ^{30}Si (Hezel and Palme, 2010; Kadlag et al., 2019b; Chaussidon et al., 2020). Thus, if a reduction of Fe^{2+} in previously oxidized chondrule silicates occurred in the solar nebula (Eq. (5)), then metal and SiO_{gas} must have been expelled from rotating chondrule melt droplets into the surrounding gas and later on, Fe metal was accreted with matrix (Hezel and Palme, 2010). In order to melt chondrule silicates and to expel the Fe-metal from chondrules, reduction of Fe silicates should have occurred at high temperatures (>1500 K). If this was the last nebular process before accretion, then the matrix composition should also be more reduced compared to type II chondrules, which is not the case. Ni/Co ratios in chondrules are about CI chondrite-like in analyses with low abundances of Ni and Co (Fig. 7) and deviate from $Ni/Co_{CI\ chondrite}$ values where Ni and Co occur in higher abundances, notably at chondrule rims. The fractionation of Ni/Co and a stronger depletion of Pt, Pd and Au relative to Ni and Co is mainly observed in the non-porphyritic and type I porphyritic chondrules (Fig. 7a and 7c and Supplementary Figs. EA4, EA5). The variation of Ni/Co near chondrule rims was explained by silicate melt-metal melt fractionation during the expulsion of the Fe-metal from chondrule melt (Palme et al., 2014). The size of metal grains in chondrules tends to increase toward the rims (Supplementary Fig. EA1). Bigger metal droplets can be removed from the rotating chondrule melt more easily (Uesugi et al., 2008), whereas smaller droplets of metal melt were trapped in the chondrules during their fast solidification. Most type I chondrules contain silicates with minor FeO and Fe-metal (Figs. 1 and 2), whereas type II chondrules contain abundant Fe-rich silicates. The latter were interpreted to have formed by oxidation of Fe_{metal} or Fe_{gas} in the solar nebula (Villeneuve et al., 2015). Higher abundances of Pt, Pd and Au in type II chondrules (Supplementary Figs. EA5 and EA6) compared to type I chondrules indicate higher abundances of primary Fe metal in type II chondrules. Thus, Fe-Ni metal-rich and -poor type chondrules likely co-existed in the nebular environment. Type II chondrules (e.g. CH#17, HSE abundances are below detection limit) were likely derived from metal-poor type I chondrules, in which forsterite reacted with FeO and formed Fe-rich olivine and pyroxene.

Thus, type I metal-rich and metal-poor chondrules were formed at high temperatures and more reducing conditions compared to CI chondrites. Type II chondrules and matrix were formed at low temperatures and oxidizing conditions by open system isotope and element exchange of nebular gas with type I chondrules. Element exchange processes further occurred during parent body metamorphism.

To summarize, the variations in the siderophile element abundances and δ^{30}Si values from this study suggest that the formation of type II chondrules due to oxidation of type I chondrules is more likely than the opposite model. The oxidation of type II chondrules likely began in the solar nebula and further continued during alteration on the

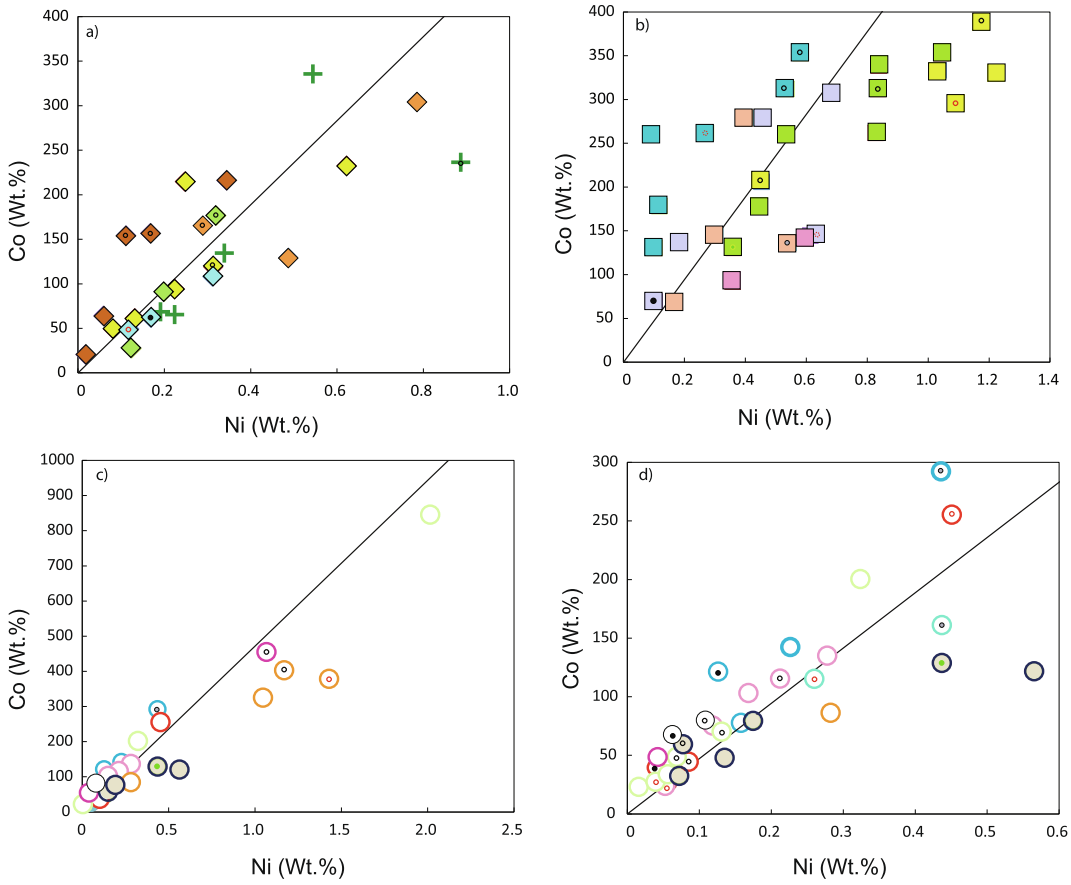

Fig. 7. Variation of Co *vs.* Ni in the analysed spots from (a) nonporphyritic chondrules, (b) type II and opaque mineral-bearing altered porphyritic chondrules, (c) type I porphyritic chondrules, and (d) enlarged view of (c). Black straight line represents CI-chondrite like Ni/Co ratios (Lodders, 2003). Deviations from the CI chondrite-like Ni/Co ratio are observed for analyses near to the rim and for analyses with higher Ni and Co concentrations.

parent body, as indicated by textural, chemical and isotopic evidence.

4.4. The influence of volatility on δ^{30}Si of chondrules

Volatility control on stable isotope fractionation can be assessed in cases where δ^{30}Si varies with ratios of volatile to refractory elements, such as K/Ca. Due to higher evaporative loss of K, K/Ca should be lower in chondrules compared to K/Ca in CI chondrites. Assuming chondrule silicates crystallized from the same reservoir by a single event involving melting, evaporation and incomplete condensation of volatile elements, a depletion of K relative to Ca and enrichment of ^{30}Si in chondrule minerals might be expected. Non-systematic scatter in δ^{30}Si and K/Ca is observed for individual analyses in chondrules (Fig. 8a and b), which suggests that at least two different chemical (K and Ca) and isotopic (for Si) reservoirs or two different processes are responsible for the chemical and isotope variation in chondrule silicates. This is also suggested by non-systematic variations of Ca/Na with δ^{30}Si within individual chondrules (Fig. 5e and 5f). Thus, the decoupling of minor elements from δ^{30}Si suggests that the isotope fractionation of Si is not directly related to the depletion of moderately volatile elements in individual chondrules. Therefore, evaporation and incomplete condensation processes related to the last chondrule formation event alone cannot account for the variability of the δ^{30}Si data.

Experimental results suggest that at high temperatures and low pressures, the partition coefficient of Ca between olivine and silicate melt is higher than the partition coefficient of K (Taura et al., 1998). Therefore, higher K/Ca (coupled to high δ^{30}Si) in forsterite from BOC CH#2 compared to mesostasis likely results from two unrelated processes. Because the olivine-melt equilibrium Si isotope fractionation is negligible (Shahar et al., 2011), the variation of Si isotopes must have been caused by fractionation of Si isotopes during gas–melt interaction. In CH#2, mesostasis (low δ^{30}Si) tends to be more strongly altered than forsterite, yet it has also lower K/Ca compared to forsterite in CH#2, indicating that these values cannot be simply related to the different degree of alteration of mesostasis and forsterite. One possibility for this discrepancy is that tiny glass inclusions in forsterite may have contributed to the higher K/Ca ratio compared to mesostasis.

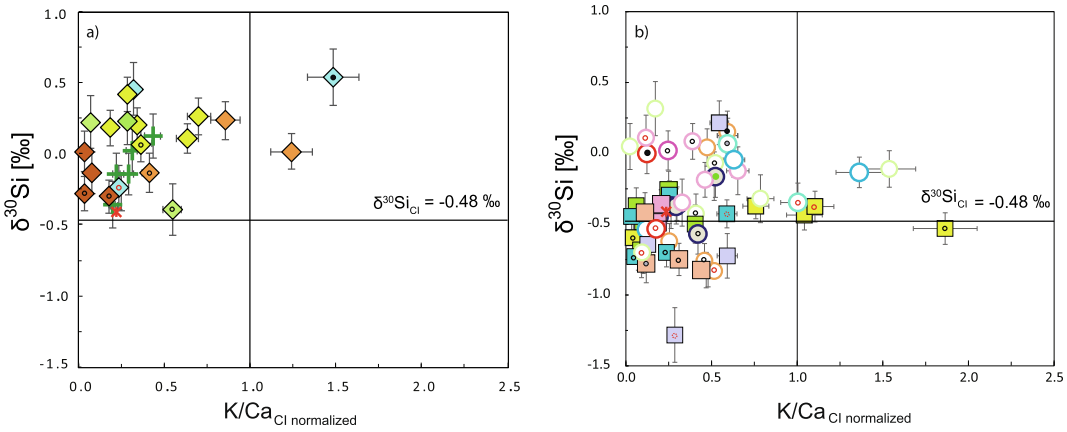

Fig. 8. Variation of δ^{30}Si *vs.* CI chondrite-normalized K/Ca (a) non-porphyritic chondrule silicates and in (b) porphyritic chondrule silicates of this study. Non-systematic variations of δ^{30}Si and K/Ca in chondrule phases may reflect differences in the volatilities of K, Ca and Si, and the different partitioning of these elements between olivine, pyroxenes and mesostasis.

The radial pyroxene chondrule CH#3 and type I PP CH#10 show a linear positive correlation of δ^{30}Si with K/Ca, and a negative correlation with Ca/Na (Fig. 5c and 8b). These elemental and isotopic differences cannot be explained only by evaporation and condensation or alteration processes. The data on RPC CH#3 suggests that heterogeneities of Si isotopes and volatile element concentrations in chondrule silicates were not established in a single evaporative or condensation event. Rapid cooling of the chondrule as indicated by its texture, permitted the preservation of internal chemical and isotopic heterogeneities (Supplementary Fig. EA1).

High K/Ca and low δ^{30}Si values in highly altered PC may result from alteration in the nebula i.e. later addition of volatile K and ^{28}Si at temperatures lower than the formation temperatures of forsterite and enstatite (Fig. 8b). These results suggest that the variable processing of chondrule precursors led to different elemental and isotopic compositions. In some cases, Si isotopes of olivine and the mesostasis were equilibrated and in other cases equilibration may have been incomplete or solid-melt-gas interaction in the solar nebula caused differences in δ^{30}Si between olivine and mesostasis. Olivine and mesostasis that are equilibrated with each other likely had similar δ^{30}Si but different K/Ca, whereas olivine and mesostasis that experienced different degrees of alteration likely had variable δ^{30}Si and K/Ca. The variation of δ^{30}Si and K/Ca in Allende chondrule silicates (Fig. 8b) suggest that both scenarios are possible.

To summarize, forsterite from chondrules of similar textures and chemical compositions from the Allende meteorite may have derived from precursors with variable (up to 0.4‰) Si isotope compositions. Alternatively, in case of BOC and type I chondrules, alteration of forsterite in chondrules due to open system isotope exchange with nebular gas may have introduced isotopic and chemical heterogeneities. The variation of δ^{30}Si in type II and highly altered opaque mineral-bearing porphyritic chondrules was likely caused by the alteration of chondrule minerals by SiO_{gas} in the solar nebula, which may have been later overprinted locally by aqueous alteration that mobilized matrix-derived components (notably Fe) on the parent body.

4.5. Silicon isotope composition of bulk chondrules: heterogeneity of precursors or mass dependent fractionation in reservoirs?

Silicon, Mg, Fe and O are the major elements in chondrule minerals. Therefore, similar mass dependent isotope fractionation of these elements should be observed in the chondrule forming processes. Stable isotope ratios of Si, Mg and Fe in chondrules vary by up to 1.5‰ (Molini-Velsko et al., 1983; Young et al., 2002, Hezel et al., 2010; Armytage et al., 2011, this work). In case of oxygen isotopes, ^{16}O-depleted and ^{16}O-enriched mineral phases are observed in Allende chondrules (Rudraswami et al., 2011). These variations were explained by isotopic heterogeneity of precursor material followed by mass dependent fractionation during the chondrule formation processes and later alteration during parent body metamorphism.

The inter-mineral variation of δ^{30}Si between mesostasis and olivine (−0.78‰) cannot reflect only equilibrium fractionation during evaporation and recondensation, because no systematic variations between δ^{30}Si and K/Ca are observed in chondrule minerals (Fig. 8b). However, the systematically low δ^{30}Si in chondrule minerals with low Mg/Fe in each chondrule suggests a role of gas–solid interaction during chondrule formation such as recondensation of Fe and isotopically light Si on crystallizing chondrules. Therefore, both, non-equilibrium and equilibrium isotope fractionation processes need to be invoked to explain the variation of δ^{30}Si in chondrules of the Allende meteorite.

The variation of δ^{30}Si with Mg/Si can help in distinguishing equilibrium and non-equilibrium fractionation effects (Dauphas et al., 2015). Forsterite (Mg/Si = 2) is the most refractory phase among the chondrule minerals and equilibrium fractionation between forsterite and gas (with fractionation factor $\alpha > 1$) results in positive correlations of δ^{30}Si with Mg/Si (Fig. 5b and e). All porphyritic chondrules fall in the δ^{30}Si-Mg/Si 'correlation range' which represents the interaction between 70–20% forsterite (formed from equilibrium condensation of nebular gas, details are given in the Supplementary Information) and 30–80% nebular gas. Individual analyses in Ch#15 suggests

that different areas of the same chondrule represent variable interaction between forsterite and Fe-rich gas.

The combined data suggests that the variation of δ^{30}Si in chondrule silicates was predominantly controlled by solid-gas equilibrium isotope fractionation during chondrule formation, later interaction of mesostasis and chondrule rims with more oxidized and ^{28}Si-rich nebular gas (non-porphyritic chondrules) and further formation of pyroxene-rich chondrules (CH#19, CH#10) by interaction of nebular gas and forsterite. Finally, local exchange of aqueous fluids from matrix during metamorphism around chondrule rims and cracks have significantly affected the δ^{30}Si of chondrule silicates.

The systematically lower δ^{56}Fe (Hezel et al., 2010), δ^{25}Mg (Young et al., 2002) and δ^{30}Si (this study) in chondrule silicates from Allende, suggests that the nebular alteration and local fluid transport during the parent body alteration mainly caused kinetic isotope fractionation between the fluid source and altered phases. Thus, high temperature solid-gas equilibrium condensation and kinetic fractionation during cooling and alteration in the nebula is needed to explain the δ^{30}Si variation of the chondrule silicates.

4.6. Implications for chondrule formation models

The main processes associated with chondrule formation were repeated melting and evaporation of precursor dust, recondensation of evaporated gas onto chondrule melt and crystallization of minerals during cooling (Connolly and Love, 1998 and references therein). All chondrule analyses from this study show mass-dependent variations in δ^{29}Si-δ^{30}Si (Tables 1 and 2), suggesting that if any initial mass-independent heterogeneities in Si isotopes were present in chondrule precursors, then they must have been erased by thermal processing and mixing processes. The observed mass-dependent variations in δ^{29}Si-δ^{30}Si could have been caused either by initial heterogeneity in the precursors stemming from equilibrium condensation between refractory solids and gas or by kinetic isotope fractionation between solid-melt-gas under non-equilibrium conditions.

If we assume that chondrule formation occurred at 10^{-3} bar and dust enrichment of 100x to 1000x, then the forsterite condensation temperature increases (from 1336 K, Lodders, 2003) to 1780 K and 1990 K, respectively (Ebel and Grossman, 2000). Assuming, solid–gas equilibrium Si isotope fractionation of gas of solar composition and 100x dust enrichment, and that nearly 60% of the Si condensed into olivine at 1780 K (Ebel and Grossman, 2000), then the δ^{30}Si of forsterite is 0.32‰ and δ^{30}Si of remaining gas is −1.0‰, which is similar to the observed δ^{30}Si variation in most silicates in this study. If nearly 80% Si condensed into olivine at 1620 K (100x dust enrichment), the δ^{30}Si of olivine is = 0.80‰ and δ^{30}Si of remaining gas is −0.80‰ (for details see Supplementary Information section 1). The δ^{30}Si of remaining gas (−0.80‰) is similar within uncertainty to the fayalite rich olivine from this study, which is the last silicate phase that might have formed by condensation in fast cooling chondrules. A fraction of the forsterite interacted with the nebular gas in an open system, as a result chondrule silicates with variable δ^{30}Si formed in the solar nebula with decreasing temperatures. Thus, the end members forsterite and gas and their interaction products can explain the δ^{30}Si values of 99% of the data (except only the lowest δ^{30}Si value of −1.28‰ from the highly altered chondrule CH#12) obtained in this study.

The systematic behavior of δ^{30}Si and Mg/Fe in chondrules (Fig. 5a and 5b) likely reflects at least two different processes, nebular and parent body alteration. At very high cooling rates, the original Si isotope composition of chondrule precursors might not have changed significantly after melting and evaporation. If the cooling rate was sufficiently low to allow the Si in the gas to interact with the crystallizing chondrule melt, then re-condensed Si would be isotopically lighter than the chondrule melt. Previous studies suggested that the Mg/Fe variation in the Allende meteorite was caused by alteration in the solar nebula (Weinbruch et al., 1990; Ikeda and Kimura, 1995; Kimura and Ikeda, 1997; Weisberg and Prinz, 1998; Hezel and Palme, 2008) and/or by hydrothermal alteration on the meteorite parent body (Housley and Cirlin, 1983; Jabeen et al., 1998; Brearley, 1999). In the former case, some Fe in chondrule rims may have been introduced by condensation of Fe from cooling gas. Low temperature hydrothermal alteration likely also resulted in an increase of the fayalite component in olivine because the release of O from water ice and subsequent oxidation of Fe-metal (Eq. (3)) to Fe^{2+}, which was incorporated in silicates, resulting in a decrease of the Mg/Fe ratio of the latter. The extent of Si isotope exchange during this process is not clear. Diffusion of Si at low temperatures is very slow in chondrule minerals, affecting a much smaller spatial scale than our analyses (Dohmen et al., 2002). However, the diffusion rate of Si in olivine is enhanced by the presence of water (Costa and Chakraborty, 2008). Thus, if Fe-rich olivine rims and veins are formed during fluid-assisted transport of matrix material during metamorphism, Si from matrix which is enriched in the light isotopes might be incorporated into chondrule rims and altered mineral phases. Therefore, the variations in the Si isotope composition in chondrule minerals near to the rims and in veins may result from a combination of nebular and parent body processes. As discussed before, the difference between type I and II chondrules is mostly a result of the higher initial metal content of type II chondrules and intense alteration of the latter (Fig. 9a).

Results from our study show that mesostasis from chondrules with similar textures show different Si isotope ratios (e.g. mesostasis-rich analyses CH#2–1 and CH#11–1 of BOC CH#2 and CH#11, respectively). These variations likely reflect variable interactions of chondrule minerals with each other and with SiO gas in the solar nebula. If Allende chondrules formed in a specific region of the solar nebula, it remains unclear why some chondrules experienced different degrees of equilibration after melting. One possibility is due to variable cooling rates. Another possibility is that the nebular disk is denser at the x-y plane of the disk compared to the z-axis and has a higher dust/gas ratio (Weidenschilling, 1980). Because high temperature chondrule formation processes should have mainly occurred in

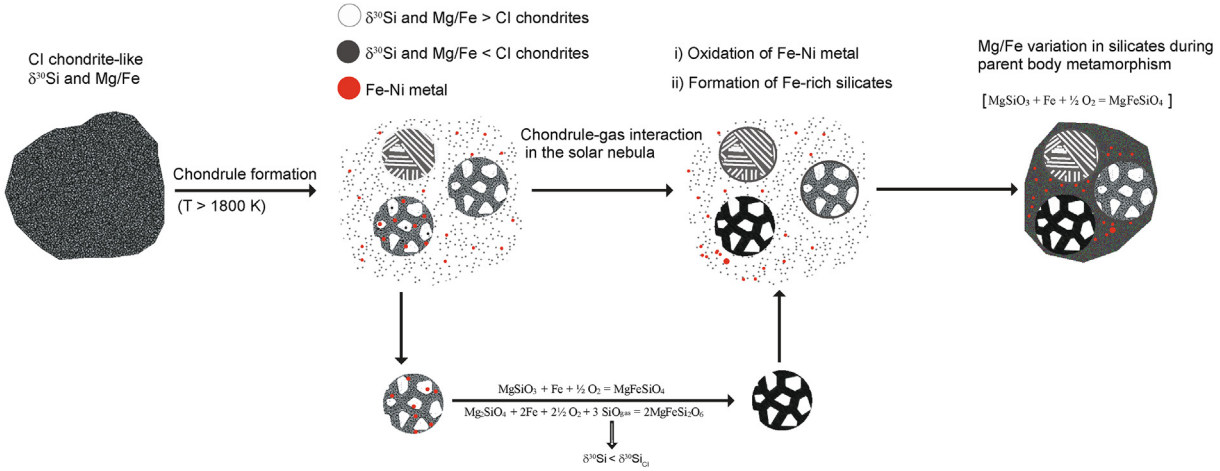

Fig. 9. Depiction of the sequence and processes of Si isotope fractionation in chondrule silicates from the Allende meteorite. The chondrule formation process produced melt from which early silicates with high δ^{30}Si and Mg/Fe crystallized. Because of evaporation of chondrule melt, the nebular gas became slightly enriched in ^{28}Si and Fe. Caused by density differences, chondrules were separated from the gas and associated dust, which may have formed a tail behind partially or fully crystallized chondrules. This early-formed 'main chondrule population' comprises non-porphyritic and porphyritic metal-poor and metal-bearing type I chondrules. Remaining evaporated material in the tail was more oxidized and richer in volatiles compared to the solidifying non-porphyritic and porphyritic type I chondrules. Interaction of this gas (specifically Fe, SiO, and O) with ^{30}Si- and Mg-rich chondrules may have formed type II chondrules and minerals with lower δ^{30}Si and Mg/Fe. Finally, parent body metamorphism may have overprinted these processes locally in altered chondrules.

the densest region of the nebula (Alexander et al., 2008; Bischoff et al. 2017; Ebel et al., 2018 and references therein), evaporated species in the gas might have separated from solids due to differential drag during their rotation around the sun. Such separation of gas may have occurred either towards the vertical (z) axis of the disk or may have followed the melt/solids (like in cometary tails) in the disk. As an effect of this separation, some earlier formed chondrules may have separated from fine dust and gas and resided in different denser clumps in the solar nebula until the movement in the disk slowed and accretion began. In such processing, different chondrules might have experienced variable equilibration of Si isotopes with remaining gas due to pressure gradient.

A schematic representation of this scenario to explain the variation of δ^{30}Si in Allende chondrules is shown in Fig. 9. The starting δ^{30}Si of Allende chondrules and matrix is assumed to be CI-chondrite-like (step 1, Fig. 9), considering the fact that the δ^{30}Si of bulk Allende (-0.41 ± 0.07‰, Armytage et al., 2011) is similar to the value of CI chondrites (-0.48 ± 0.09‰). The chondrule formation event melted the precursor dust and initially forsterite-rich barred olivine chondrules, and type I porphyritic (metal-poor and metal-rich) chondrules were formed (step 2). The forsterite in such chondrules shows high δ^{30}Si of up to 0.55‰, as an effect of the equilibrium fractionation between initially crystallized forsterite and gas at high temperature (>1700 K). The highest δ^{30}Si, Mg/Fe and Mg/Si are recorded in olivine of these chondrules. The remaining nebular gas became more oxidizing with decreasing temperatures at this stage. Type II and pyroxene-rich chondrules formed during the interaction with ^{28}Si-rich SiO gas and earlier formed solid forsterite (step 3). The earlier formed metal-rich chondrules begin to oxidize at more oxidising conditions prior to the accretion of chondrule rims and matrix (as described in equations (3) and (4)). Mediated by gas, the Fe-metal from metal-rich chondrules is reacting with enstatite and forsterite to form Fe-rich solid solutions. Reactions and isotope exchange with nebular gas occur under open system conditions. Furthermore, after the accretion of chondrules, matrix and ices to the Allende parent body, melting of ice and open-system alteration with the aqueous fluids on the parent body resulted in the local decrease of δ^{30}Si, Mg/Fe and Mg/Si of some chondrule silicates (step 4). Accretion of most of the mass from the same orbit into specific chondrite parent bodies might explain the limited variations in δ^{30}Si and element ratios in the different types of chondrules and matrix, yet maintaining the complementarity of these 'sub-reservoirs' as indicated by CI chondrite-like ratios of specific elements and isotopes observed in the bulk rock of the Allende meteorite (Palme et al., 1992, 2015; Bland et al., 2005; Dohmen et al., 2002; Hezel and Palme, 2008, 2010, Budde et al., 2016a, 2016b; Kadlag et al., 2019c).

To summarize, the Si isotope and element variations in the chondrule minerals of the Allende meteorite are best explained by heating and fractional crystallization processes that occurred in the same heliocentric orbit at different times and presumably at different locations. Short-term heat sources for the melting of dust to form chondrules could have been supplied by shocks driven by gravitational instability, planetesimals bow shocks or solar nebula lightning (Iida et al., 2001; Ciesla and Hood, 2002; Desch and Connolly, 2002; Morris and Desch, 2010).

5. CONCLUSIONS

The variation of δ^{30}Si values and major, minor and trace element abundances in chondrule silicates determined at

high spatial resolution reveal the processing of chondrules in the solar nebula as well as on the Allende meteorite parent body.

The variation of δ^{30}Si in chondrule silicates is less controlled by the spatial position or chondrule size, but is related to variations of the Mg/Fe ratio. Mg-rich olivine and pyroxene in chondrules show higher δ^{30}Si compared to Fe-rich olivine and pyroxene in the same chondrule. The extent of depletion of volatile elements from chondrules (inferred from K/Ca) is independent of the Si isotope fractionation of chondrule minerals. The limited variation in δ^{30}Si (up to 1.8‰) in the chondrules, low δ^{30}Si in Fe-rich phases and the correlation of δ^{30}Si with Mg/Fe and Mg/Si suggests that in some non-porphyritic chondrules the variation of δ^{30}Si was predominantly controlled by kinetic isotope fractionation during gas-melt/solid interaction, whereas in porphyritic chondrules equilibrium isotope fractionation was the dominant process. Thus, the variations of δ^{30}Si and Mg/Fe ratios in different chondrules resulted from the modification of chondrules in the solar nebula, and, to variable extent, during later parent body alteration in case of rims and altered phases with low Mg/Fe.

The limited variation of δ^{30}Si in chondrule minerals suggests that after evaporation of the chondrule melt at nebular dust/gas ratios, >90% of the Si was condensed back onto the crystallizing chondrule melt. Alternatively, evaporation of chondrule silicates occurred at high dust/gas ratios (>100 times nebular value), which prevented the kinetic isotope fractionation of chondrule precursors, due to a higher ratio of ablation rate to diffusion rate (Young et al., 1998).

The higher δ^{30}Si values in BOC silicates compared to PC silicates are consistent with the higher cooling rates of BOC compared to PC (Lofgren, 1989), reflecting differences in Si isotope fractionation during evaporation/condensation processes during the formation of these different chondrule types. The relationships with textures suggest that the variation of δ^{30}Si between different types of chondrules is predominantly a nebular process which can be explained by different extents of equilibrium and kinetic isotope fractionation of Si isotopes during heating and cooling. Mg-rich olivine with high δ^{30}Si compared to CI chondrites reacted with Fe and SiO (that has a low δ^{30}Si compared to CI chondrites) in the gas and formed less refractory and ^{30}Si-depleted silicates.

Combined evidence from REE abundances and δ^{30}Si values in mesostasis suggests that the mesostasis continued to interact with the nebular gas after higher partitioning of REE into melt (that formed mesostasis) compared to solids (e.g. olivine). Higher enrichment of siderophile elements towards chondrule rims and the variation in the Pt/Pd and Ni/Co ratios in different chondrules provides further evidence for the expulsion of Fe-Ni metal, during chondrule formation.

In summary, our *in situ* analyses of element concentrations and Si isotope ratios within 21 chondrules from a small area (ca. 4.9 cm^2) of the Allende meteorite reveal the complex formation histories of chondrules. The composition of some chondrules require variable maximum temperatures or variable heating duration and cooling rates and a variety of interactions of the chondrule minerals with the nebular gas and further aqueous alteration on the parent body. The complementary variations of Mg/Fe and δ^{30}Si in type I and type II chondrules compared to the matrix (Kadlag et al., 2019; Chaussidon et al., 2020) suggests that chondrules and matrix of Allende likely formed from same reservoir in the solar nebula. These relationships further suggest that Allende chondrules were formed by heating of dust in the solar nebula and are not products of planetesimal collisions.

Declaration of Competing Interest

The authors declare that they have no known competing financial interests or personal relationships that could have appeared to influence the work reported in this paper.

ACKNOWLEDGEMENTS

We thank R. Milke, and A. Giribaldi (both FUB), C. Günter (Potsdam University), J. Buhk and J. Schüssler (both GFZ Potsdam) for help during sample preparation, EPMA and MC-ICP-MS analysis. Special thanks to F. von Blanckenburg for supporting this work. We also thank D. Hezel, two anonymous reviewers and associate editor, S. Russel for their thorough and constructive comments, which have been very helpful in improving the manuscript. D.A.F. likes to thank Marie Curie initial training network IsoNose (www.IsoNose.eu) that is funded by the Marie Curie Actions Programme of the European Union's Seventh Framework Programme (FP7/2007-2013/ under REA grant agreement No 608069). This work and a fellowship to M.T. were funded by DFG (SFB-TRR 170 "Late accretion onto terrestrial planets") and FUB funds. This is TRR publication number 134.

APPENDIX A. SUPPLEMENTARY MATERIAL

Supplementary data to this article can be found online at https://doi.org/10.1016/j.gca.2021.04.022.

REFERENCES

Alexander C.M.O'D., Grossman J. N., Ebel D. S., and Ciesla F. J. (2008) The formation conditions of chondrules and chondrites. Science, 320(5883), 1617-1619

Armytage R. M. G. (2011) *The silicon isotopic composition of inner Solar System materials* (PhD thesis). Oxford University, UK.

Armytage R. M. G., Georg R. B., Savage P. S., Williams H. M. and Halliday A. N. (2011) Silicon isotopes in meteorites and planetary core formation. *Geochim. Cosmochim. Acta* **75**, 3662–3676.

Armytage R. M. G., Georg R. B., Williams H. M. and Halliday A. N. (1800) Silicon isotopic composition of CV3 chondrules and isotopic fractionation in the solar nebula. *LPICo* **77**(1800), 5128.

Barosch J., Hezel D. C., Sawatzki L., Halbauer L. and Marrocchi Y. (2020) Sectioning effects of porphyritic chondrules: Implications for the PP/POP/PO classification and correcting modal abundances of mineralogically zoned chondrules. *Meteorit. Planet. Sci.* **55**(5), 993–999.

Birle J. D., Gibbs G. V., Moore P. B. and Smith J. V. (1968) Crystal structures of natural olivines. *Am. Mineral.* **53**, 807–824.

Bischoff A., Wurm G., Chaussidon M., Horstmann M., Metzler K., Weyrauch M. and Weinauer J. (2017) The Allende multicompound chondrule (ACC)—Chondrule formation in a local super-dense region of the early solar system. *Meteoritics Planet. Sci.* **52**(5), 906–924.

Bland P. A., Alard O., Benedix G. K., Kearsley A. T., Menzies O. N., Watt L. E. and Rogers N. W. (2005) Volatile fractionation in the early solar system and chondrule/matrix complementarity. *Proceedings of the National Academy of Sciences* **102**(39), 13755–13760.

Bonal L., Quirico E., Bourot-Denise M. and Montagnac G. (2006) Determination of the petrologic type of CV3 chondrites by Raman spectroscopy of included organic matter. *Geochim. Cosmochim. Acta* **70**(7), 1849–1863.

Brearley A. J. (1999) Origin of graphitic carbon and pentlandite in matrix olivines in the Allende meteorite. *Science* **285**(5432), 1380–1382.

Boss A. P. (1996) A concise guide to chondrule formation models. *Chondrules and the Protoplanetary Disk* **27**, pp257.

Budde G., Kleine T., Kruijer T. S., Burkhardt C. and Metzler K. (2016) Tungsten isotopic constraints on the age and origin of chondrules. *Proc. Natl. Acad. Sci.* **113**(11), 2886–2891.

Chakrabarti R. and Jacobsen S. B. (2010) Silicon isotopes in the inner Solar System: implications for core formation, solar nebular processes and partial melting. *Geochim. Cosmochim. Acta* **74**, 6921–6933.

Chaussidon M., Libourel G. and Krot A. N. (2008) Oxygen isotopic constraints on the origin of magnesian chondrules and on the gaseous reservoirs in the early Solar System. *Geochim. Cosmochim. Acta* **72**, 1924–1938.

Chaussidon M., Martins Pimentel R., Deng Z., and Moynier F. (2020) Mass-dependent silicon isotope fractionation among allende components: Implications on genetic relationships and complementarity. In Lunar and Planetary Science Conference (No. 2326, p. 1396).

Ciesla F. J. and Hood L. L. (2002) The nebular shock wave model for chondrule formation: Shock processing in a particle–gas suspension. *Icarus* **158**(2), 281–293.

Clayton R. N., Mayeda T. K., Molini-Velsko C. A. and Goswami J. N. (1983) Oxygen and silicon isotopic composition of Dhajala chondrules. *Meteoritics* **18**, 282.

Cohen B. A., Hewins R. H. and Alexander C. M. O'D. (2004) The formation of chondrules by open-system melting of nebular condensates. *Geochim. Cosmochim. Acta* **68**, 1661–1675.

Costa F. and Chakraborty S. (2008) The effect of water on Si and O diffusion rates in olivine and implications for transport properties and processes in the upper mantle. *Phys. Earth Planet. Inter.* **166**(1–2), 11–29.

Dauphas N., Poitrasson F., Burkhardt C., Kobayashi H. and Kurosawa K. (2015) Planetary and meteoritic Mg/Si and δ30Si variations inherited from solar nebula chemistry. *Earth Planet. Sci. Lett.* **427**, 236–248.

Desch S. J. and Connolly, Jr., H. C. (2002) A model of the thermal processing of particles in solar nebula shocks: Application to the cooling rates of chondrules. *Meteoritics Planet. Sci.* **37**(2), 183–207.

Desch S. J., Morris M. A., Connolly, Jr., H. C. and Boss A. P. (2012) The importance of experiments: Constraints on chondrule formation models. *Meteorit. Planet. Sci.* **47**(7), 1139–1156.

Ebel D. S. and Grossman L. (2000) Condensation in dust-enriched systems. *Geochim. Cosmochim. Acta* **64**(2), 339–366.

Dohmen R., Chakraborty S. and Becker H. W. (2002) Si and O diffusion in olivine and implications for characterizing plastic flow in the mantle.. *Geophys. Res. Lett.* **29**(21), 26–1–26–4.

Ebel D. S., Alexander C. M. O. D. and Libourel G. (2018) *Vapor–melt exchange*. Records of Protoplanetary Disk Processes. Cambridge University Press, Cambridge, Chondrules, pp. 151–174.

Frick D. A., Schuessler J. A. and von Blanckenburg F. (2016) Development of routines for simultaneous *in situ* chemical composition and stable Si isotope ratio analysis by femtosecond laser ablation inductively coupled plasma mass spectrometry. *Anal. Chim. Acta* **938**, 33–43.

Friend P., Hezel D. C. and Mucerschi D. (2016) The conditions of chondrule formation, Part II: Open system. *Geochim. Cosmochim. Acta* **173**, 198–209.

Fitoussi C., Bourdon B., Kleine T., Oberli F. and Reynolds B. C. (2009) Si isotope systematics of meteorites and terrestrial peridotites: implications for Mg/Si fractionation in the solar nebula and for Si in the Earth's core. *Earth Planet. Sci. Lett.* **287**, 77–85.

Galy A., Young E. D., Ash R. D. and O'Nions R. K. (2000) The formation of chondrules at high gas pressures in the solar nebula. *Science* **290**(5497), 1751–1753.

Georg R. B., Halliday A. N., Schauble E. A. and Reynolds B. C. (2007) Silicon in the Earth's core. *Nature* **447**, 1102–1106.

Gooding J. L. and Keil K. (1981) Relative abundances of chondrule primary textural types in ordinary chondrites and their bearing on conditions of chondrule formation. *Meteoritics* **16**(1), 17–43.

Guimon R. K., Symes S. J., Sears D. W. and Benoit P. H. (1995) Chemical and physical studies of type 3 chondrites XII: The metamorphic history of CV chondrites and their components. *Meteoritics* **30**(6), 704–714.

Harju E. R. (2015) Aqueous alteration and silicon and magnesium isotope measurements in CR and CV chondrites (Doctoral dissertation, UCLA).

Hewins R. H., Klein L. C., and Fasano B. V. (1981) Conditions of formation of pyroxene excentroradial chondrules. In Lunar and Planetary Science Conference (Vol. 12, pp. 448-450).

Hertwig A. T., Defouilloy C. and Kita N. T. (2018) Formation of chondrules in a moderately high dust enriched disk: Evidence from oxygen isotopes of chondrules from the Kaba CV3 chondrite. *Geochim. Cosmochim. Acta* **224**, 116–131.

Hewins R. H., Connolly H. C., Lofgren, Jr., G. E. and Libourel G. (2005) Experimental constraints on chondrule formation. *Chondrites and the Protoplanetary Disk* **341**, 286.

Hezel D. C. and Palme H. (2008) Constraints for chondrule formation from Ca–Al distribution in carbonaceous chondrites. *Earth Planet. Sci. Lett.* **265**(3–4), 716–725.

Hezel D. C. and Palme H. (2010) The chemical relationship between chondrules and matrix and the chondrule matrix complementarity. *Earth Planet. Sci. Lett.* **294**(1–2), 85–93.

Hezel D. C., Needham A. W., Armytage R., Georg B., Abel R. L., Kurahashi E., Coles B. J., Rehkämper M. and Russell S. S. (2010) A nebula setting as the origin for bulk chondrule Fe isotope variations in CV chondrites. *Earth Planet. Sci. Lett.* **296**, 423–433.

Housley R. M., and Cirlin E. H. (1983) On the alteration of Allende chondrules and the formation of matrix. In Chondrules and their Origins (pp. 145-161).

Hua X., Adam J., Palme H. and El Goresy A. (1988) Fayalite-rich rims, veins, and halos around and in forsteritic olivines in CAIs and chondrules in carbonaceous chondrites: Types, compositional profiles and constraints of their formation. *Geochim. Cosmochim. Acta* **52**(6), 1389–1408.

Huang F., Zhongqing W, Huang Shichu and Fei W (2014) First-principles calculations of equilibrium silicon isotope fractionation among mantle minerals. *Geochim. Cosmochim. Acta* **140**, 509–520.

Huss G. R. and Lewis R. S. (1994) Noble gases in presolar diamonds II: Component abundances reflect thermal processing. *Meteoritics* **29**(6), 811–829.

Iida A., Nakamoto T., Susa H. and Nakagawa Y. (2001) A shock heating model for chondrule formation in a protoplanetary disk. *Icarus* **153**(2), 430–450.

Ikeda Y. and Kimura M. (1995) Anhydrous alteration of Allende chondrules in the solar nebula I: Description and alteration of chondrules with known oxygen isotopic compositions. *Antarct. Meteor. Res.* **8**, 97.

Jabeen I., Kusakabe M., Nagao K. and Nakamura T. (1998) Oxygen isotope study of Tsukuba chondrite, some HED meteorites and Allende chondrules. *Antarct. Meteor. Res.* **11**, 122.

Jacquet E., Alard O. and Gounelle M. (2012) Chondrule trace element geochemistry at the mineral scale. *Meteoritics Planet. Sci.* **47**(11), 1695–1714.

Jarosewich E., Clarke, Jr., R. S. and Barrows J. N. (1987) Allende meteorite reference sample. *Smithson. Contrib. Earth Sci.*.

Javoy M., Balan E., Méheut M., Blanchard M. and Lazzeri M. (2012) First-principles investigation of equilibrium isotopic fractionation of O-and Si-isotopes between refractory solids and gases in the solar nebula. *Earth Planet. Sci. Lett.* **319**, 118–127.

Jochum K. P., Nohl U., Herwig K., Lammel E., Stoll B. and Hofmann A. W. (2005) GeoReM: A new geochemical database for reference materials and isotopic standards. *Geostand. Geoanalytical Res.* **29**(3), 333–338.

Jochum K. P., Weis U., Stoll B., Kuzmin D., Yang Q., Raczek I., Jacob D. E., Stracke A., Birbaum K., Frick D. A., Günther D. and Enzweiler J. (2011) Determination of reference values for NIST SRM 610–617 glasses following ISO guidelines. *Geostand. Geoanalytical Res.* **35**(4), 397–429.

Jones R. H. and Danielson L. R. (1997) A chondrule origin for dusty relict olivine in unequilibrated chondrites. *Meteoritics Planet. Sci.* **32**(6), 753–760.

Jones R. H., Grossman J. N., and Rubin A. E. (2005) Chemical, mineralogical and isotopic properties of chondrules: Clues to their origin. In Chondrites and the protoplanetary disk (Vol. 341, p. 251).

Johnson B. C., Minton D. A., Melosh H. J. and Zuber M. T. (2015) Impact jetting as the origin of chondrules. *Nature* **517**(7534), 339–341.

Kadlag Y., Tatzel M., Frick D. A. and Becker H. (2019a) The origin of unequilibrated EH chondrites–Constraints from in situ analysis of Si isotopes, major and trace elements in silicates and metal. *Geochim. Cosmochim. Acta* **267**, 300–321.

Kadlag Y., Tatzel M., Frick D. A., Becker H., and Kühne P. (2019b) Chondrule-matrix complementarity in the allende CV3 chondrite-A Si isotope perspective. In Lunar and Planetary Science Conference (Vol. 50) abstr#1092.

Kadlag Y., Becker H. and Harbott A. (2019c) Cr isotopes in physically separated components of the Allende CV3 and Murchison CM2 chondrites: Implications for isotopic heterogeneity in the solar nebula and parent body processes. *Meteoritics Planet. Sci.* **54**(9), 2116–2131.

Kereszturi A., Blumberger Z., Józsa S., May Z., Müller A., Szabó M. and Tóth M. (2014) Alteration processes in the CV chondrite parent body based on analysis of NWA 2086 meteorite. *Meteoritics Planet. Sci.* **49**(8), 1350–1364.

Kimura M. and Ikeda Y. (1997) Comparative study of anhydrous alteration of chondrules in reduced and oxidized CV chondrites. *Antarct. Meteor. Res.* **10**, 191.

Krot A. N., Fagan T. J., Keil K., McKeegan K. D., Sahijpal S., Hutcheon I. D., Petaev M. I. and Yurimoto H. (2004a) Ca, Al-rich inclusions, amoeboid olivine aggregates, and Al-rich chondrules from the unique carbonaceous chondrite Acfer 094: I. mineralogy and petrology. *Geochim. Cosmochim. Acta* **68**(9), 2167–2184.

Krot A. N., Libourel G., Goodrich C. A. and Petaev M. I. (2004b) Silica-rich igneous rims around magnesian chondrules in CR carbonaceous chondrites: Evidence for condensation origin from fractionated nebular gas. *Meteorit. Planet. Sci.* **39**(12), 1931–1955.

Krot A. N., Petaev M. I., Scott E. R. D., CHOI B. G., Zolensky M. E. and Keil K. (1998) Progressive alteration in CV3 chondrites: More evidence for asteroidal alteration. *Meteoritics & Planetary Science* **33**(5), 1065–1085.

Krot A. N., Scott E. R. D. and Zolensky M. E. (1997) Origin of fayalitic olivine rims and lath-shaped matrix olivine in the CV3 chondrite Allende and its dark inclusions. *Meteoritics and Planetary Science,* **32**(1), 31–49.

Lemelle L., Guyot F., Leroux H. and Libourel G. (2001) An experimental study of the external reduction of olivine single crystals. *Am. Mineral.* **86**(1–2), 47–54.

Leroux H., Libourel G., Lemelle L. and Guyot F. (2003) Experimental study and TEM characterization of dusty olivines in chondrites: Evidence for formation by in situ reduction. *Meteoritics Planet. Sci.* **38**(1), 81–94.

Lewis J. A. and Jones R. H. (2019) Primary feldspar in the Semarkona LL 3.00 chondrite: Constraints on chondrule formation and secondary alteration. *Meteorit. Planet. Sci.* **54**(1), 72–89.

Libourel G. and Chaussidon M. (1995) Experimental constraints on chondrule reduction. *Meteoritics* **30**.

Libourel G., Krot A. N. and Tissandier L. (2006) Role of gas-melt interaction during chondrule formation. *Earth Planet. Sci. Lett.* **251**(3–4), 232–240.

Lodders K. (2003) Solar system abundances and condensation temperatures of the elements. *Astrophys. J.* **591**(2), 1220.

Lofgren G. and Russell W. J. (1986) Dynamic crystallization of chondrule melts of porphyritic and radial pyroxene composition. *Geochim. Cosmochim. Acta* **50**(8), 1715–1726.

Lofgren G. (1989) Dynamic cyrstallization of chondrule melts of porphyritic olivine composition: textures experimental and natural. *Geochim. Cosmochim. Acta* **53**(2), 461–470.

McSween, Jr., H. Y. (1977) Chemical and petrographic constraints on the origin of chondrules and inclusions in carbonaceous chondrites. *Geochim. Cosmochim. Acta* **41**(12), 1843–1860.

Méheut M., Lazzeri M., Balan E. and Mauri F. (2009) Structural control over equilibrium silicon and oxygen isotopic fractionation: A first-principles density-functional theory study. *Chem. Geol.* **258**, 28–37.

Méheut M. and Schauble E. A. (2014) Silicon isotope fractionation in silicate minerals: insights from first-principles models of phyllosilicates, albite and pyrope. *Geochim. Cosmochim. Acta* **134**, 137–154.

Misawa K. and Nakamura N. (1988) Demonstration of REE fractionation among individual chondrules from the Allende (CV3) chondrite. *Geochim. Cosmochim. Acta* **52**(6), 1699–1710.

Morris M. A. and Desch S. J. (2010) Thermal histories of chondrules in solar nebula shocks. *Astrophys. J.* **722**(2), 1474–1494.

Molini-Velsko C., Mayeda T. K., and Clayton R. N. (1983) Silicon isotopes in components of the Allende meteorite. In Lunar and Planetary Science Conference (Vol. 14, pp. 509-510)

Nielsen R. L., Gallahan W. E. and Newberger F. (1992) Experimentally determined mineral-melt partition coefficients for Sc, Y and REE for olivine, orthopyroxene, pigeonite, magnetite and ilmenite. *Contrib. Miner. Petrol.* **110**(4), 488–499.

Olsen M. B., Wielandt D., Schiller M., Van Kooten E. M. and Bizzarro M. (2016) Magnesium and 54Cr isotope compositions

of carbonaceous chondrite chondrules–Insights into early disk processes. *Geochim. Cosmochim. Acta* **191**, 118–138.
Palme H., Hezel D. C. and Ebel D. S. (2015) The origin of chondrules: Constraints from matrix composition and matrix-chondrule complementarity. *Earth Planet. Sci. Lett.* **411**, 11–19.
Palme H., Spettel B. and Hezel D. (2014) Siderophile elements in chondrules of CV chondrites. *Chemie der Erde-Geochemistry* **74** (3), 507–516.
Palme H., Spettel B., Kural G. and Zinner E. (1992) Origin of Allende chondrules. *Lunar Planet. Sci. Conf.* **23**.
Pringle E. A., Moynier F., Beck P., Paniello R. and Hezel D. C. (2017) The origin of volatile element depletion in early solar system material: Clues from Zn isotopes in chondrules. *Earth Planet. Sci. Lett.* **468**, 62–71.
Qin T., Wu F., Wu Z. and Huang F. (2016) First-principles calculations of equilibrium fractionation of O and Si isotopes in quartz, albite, anorthite, and zircon. *Contrib. Miner. Petrol.* **171** (11), 91.
Rudraswami N. G., Ushikubo T., Nakashima D. and Kita N. T. (2011) Oxygen isotope systematics of chondrules in the Allende CV3 chondrite: high precision ion microprobe studies. *Geochim. Cosmochim. Acta* **75**(23), 7596–7611.
Ruzicka A., Floss C. and Hutson M. (2008) Relict olivine grains, chondrule recycling, and implications for the chemical, thermal, and mechanical processing of nebular materials. *Geochim. Cosmochim. Acta* **72**(22), 5530–5557.
Savage P. S., Georg R. B., Armytage R. M. G., Williams H. M. and Halliday, A. N., et al. (2010) Silicon isotope homogeneity in the mantle. *Earth Planet. Sci. Lett.* **295**(1–2), 139–146.
Savage P. S. and Moynier F. (2013) Silicon isotopic variation in enstatite meteorites: clues to their origin and Earth-forming material. *Earth Planet. Sci. Lett.* **361**, 487–496.
Sears D. W., Huang S. and Benoit P. H. (1996) Open-System Behaviour During Chondrule Formation. In *Chondrules and the protoplanetary disk*, p. 221.
Schrader D. L., Connolly, Jr, H. C. and Lauretta D. S. (2008) Opaque phases in type-II chondrules from CR2 chondrites: Implications for CR parent body formation. *Geochim. Cosmochim. Acta* **72**(24), 6124–6140.
Schuessler J. A. and von Blanckenburg F. (2014) Testing the limits of micro-scale analyses of Si stable isotopes by femtosecond laser ablation multicollector inductively coupled plasma mass spectrometry with application to rock weathering. *Spectrochim. Acta, Part B* **98**, 1–18.
Scott E. R. D. and Krot A. N. (2003) Chondrites and their components. *Treatise Geochem.* **1**, 711.
Shahar A., Hillgren V. J., Young E. D., Fei Y., Macris C. A. and Deng L. (2011) High-temperature Si isotope fractionation between iron metal and silicate.. *Geochim. Cosmochim. Acta* **75**(23), 7688–7697.
Shu F. H., Shang H., Glassgold A. E. and Lee T. (1997) X-rays and fluctuating X-winds from protostars. *Science* **277**(5331), 1475–1479.
Tatzel M., von Blanckenburg F., Oelze M., Schuessler J. A. and Bohrmann G. (2015) The silicon isotope record of early silica diagenesis. *Earth Planet. Sci. Lett.* **428**, 293–303.
Taura H., Yurimoto H., Kurita K. and Sueno S. (1998) Pressure dependence on partition coefficients for trace elements between olivine and the coexisting melts.. *Phys. Chem. Miner.* **25**(7), 469–484.
Tissandeer L., Libourel G. and Robert F. (2002) Gas-melt interactions and their bearing on chondrule formation. *Meteoritics Planet. Sci.* **37**(10), 1377–1389.
Urey H. C. (1947) The thermodynamic properties of isotopic substances. *J. Chem. Soc. (Resumed)*, 562–581.
Uesugi M., Sekiya M. and Nakamura T. (2008) Kinetic stability of a melted iron globule during chondrule formation. I. Non-rotating model. *Meteorit. Planet. Sci.* **43**(4), 717–730.
Villeneuve J., Libourel G. and Soulié C. (2015) Relationships between type I and type II chondrules: Implications on chondrule formation processes. *Geochim. Cosmochim. Acta* **160**, 277–305.
Villeneuve J., Marrocchi Y. and Jacquet E. (2020) Silicon isotopic composition of silicates in carbonaceous chondrites and the formation of primordial solids in the accretion disk. *Earth and Planetary Science Letters* **542**, 116318.
Weidenschilling S. J. (1980) Dust to planetesimals: Settling and coagulation in the solar nebula. *Icarus* **44**(1), 172–189.
Weinbruch S., Palme H., Müller W. F. and El Goresy A. (1990) FeO-rich rims and veins in Allende forsterite: Evidence for high temperature condensation at oxidizing conditions. *Meteoritics* **25**(2), 115–125.
Weisberg M. K. and Prinz M. (1998) Fayalitic olivine in CV3 chondrite matrix and dark inclusions: A nebular origin. *Meteoritics Planet. Sci.* **33**(5), 1087–1099.
Young E. D., Nagahara H., Mysen B. O. and Audet D. M. (1998) Non-Rayleigh oxygen isotope fractionation by mineral evaporation: Theory and experiments in the system SiO_2. *Geochim. Cosmochim. Acta* **62**(18), 3109–3116.
Young E. D., Ash R. D., Galy A. and Belshaw N. S. (2002) Mg isotope heterogeneity in the Allende meteorite measured by UV laser ablation-MC-ICPMS and comparisons with O isotopes. *Geochim. Cosmochim. Acta* **66**(4), 683–698.
Zambardi T. and Poitrasson F. (2010) Precise Determination of Silicon Isotopes in Silicate Rock Reference Materials by MC-ICP-MS. *Geostand. Geoanal. Res.* **35**, 89–99.
Zambardi T., Poitrasson F., Corgne A., Méheut M., Quitte´ G. and Anand M. (2013) Silicon isotope variations in the inner solar system: implications for planetary formation, differentiation and composition. *Geochim. Cosmochim. Acta* **121**, 67–83.

Associate editor: Sara S. Russell